Applied Surface Science 611 (2023) 155538

Contents lists available at ScienceDirect

Applied Surface Science

journal homepage: www.elsevier.com/locate/apsusc

Full length article

Multi-pulse agglomeration effects on ultrashort pulsed direct laser interference patterning of Cu

Daniel Wyn Müller [a,*], Sarah Lößlein [a], Christoph Pauly [a], Max Briesenick [b], Guido Kickelbick [b], Frank Mücklich [a]

[a] Chair of Functional Materials, Department of Materials Science, Saarland University, 66123 Saarbrücken, Germany
[b] Department of Inorganic Solid-State Chemistry, Elemental Analysis, Saarland University, 66123 Saarbrücken, Germany

ARTICLE INFO

Keywords:
Direct laser interference patterning
Ultrashort laser pulses
Biomimetic surface structures
Functional surfaces

ABSTRACT

Surface functionalization by biomimetic patterns in the micro- and nanometer scale is well-established in a wide range of applications. The finely tuned surface properties are directly related to both primary and sub-pattern morphology of the applied topographies, which must be well-adjusted for maximum functionalization efficiency. In this light, the role of proceeding surface modification and its effect on pattern formation alongside multi-pulse ultrashort pulsed direct laser interference patterning (USP-DLIP) of Cu are investigated in detail by applying a multi-method characterization approach. It was shown that aside of topographical remodeling, USP-DLIP processing parallelly affects chemistry and the mechanical deformation state of the substrate surface, which in turn considerably influences laser/material interaction via incubation. An in-depth investigation of the individual and combined impacts of these substrate alterations on localized optical absorptance reveals how primary and sub-pattern formation dynamically respond to process induced surface modification. The DLIP-specific incubation impact on pattern morphology increases with inverted relation to pattern scale. The findings of this study provide a profound insight in the predominant physical interactions involved in pattern formation arising from the mutual influence between laser irradiation and substrate modification during USP-DLIP-processing of Cu allowing for high precision micro- and nanometer scaled pattern design.

1. Introduction

Surface patterning in the micro- and nanometer scale mimicking natural blue prints found in manifold variation in the flora and fauna has been well-applied and developed to improve technical surface properties in the last two decades [1]. The envisaged application areas cover a broad spectrum from optical effects and photonics [2],[3], to technically utilized surface functionalization including wetting, friction and wear [4–6], as well as biomedical surface optimization to enhance cell colonization or antibacterial surface properties in the civil and aerospace sector [7–10]. Here, a close connection between sophisticated pattern design and effectiveness of the surface functionalization was demonstrated across the different applications studied, which is highlighting the necessity to understand and precisely control the process of pattern formation.

Among the technologies applied in this field, pulsed laser irradiation in the pico- and femtosecond regime involving purposefully induced interference has proven to be particularly versatile in terms of precision and variety of pattern geometries that can be created [11],[12]. In direct laser interference patterning (DLIP), the primary geometry of the topographical pattern applied is controlled by the design of the laser setup involving beam count and incidence angle, the wavelength as well as single beam polarization [13],[14]. Pattern formation itself is influenced by the material specific physical response to laser irradiation e.g. involving melt formation, vapor recoil pressure and Marangoni convection in case of pulse durations of several tens of picoseconds and higher [15], while ultrashort pulse durations <10 ps (USP) induce surface modifications dominated by varying material specific ablation mechanisms, which are closely related to individual threshold fluences [16]. Applying USP-DLIP, high aspect ratios as well as the formation of sophisticated pattern geometries can be achieved via multi-pulse overlap. However, material specific accumulation effects on pattern formation have to be considered, which might also lead to pattern deterioration as previously shown for pattern scales in the sub-µm range

* Corresponding author at: Chair of Functional Materials, Saarland University, Post Office Box 151150, 66041 Saarbruecken, Germany.
E-mail address: daniel.mueller@uni-saarland.de (D.W. Müller).

https://doi.org/10.1016/j.apsusc.2022.155538
Received 18 August 2022; Received in revised form 27 October 2022; Accepted 28 October 2022
Available online 3 November 2022

[16],[17]:

Alongside primary pattern formation, multi-pulse USP processing involves sub-pattern alteration, e.g. by self-assembly of laser induced periodic sub-structures (LIPSS) on metals, semi-conductors and dielectrics [18]. LIPSS are divided in two subspecies with different relation to beam polarization: While the formation of high spatial frequency LIPSS (HSFL, oriented parallel to beam polarization and scaling $< \lambda/2$) have been shown to mainly involve melt kinetics like Marangoni convection, low spatial frequency LIPSS (LSFL, oriented perpendicular to beam polarization and scaled $> \lambda/2$) are shaped in multi-pulse overlaps by a combination of the interference between the incident laser beam and excited surface plasmon polaritons (SPP) on a roughened surface and further increased absorption in the resulting pits, according to current theories [19],[20]. Alongside USP-DLIP, LIPSS formation can even be purposefully superimposed with the primary DLIP pattern [21], [22]. Overlying process mechanisms may suppress LIPSS formation in some cases, resulting in other forms of sub-patterns, like e.g. crater-like morphologies in the case of Cu as a result from ablation kinetics, which are also subject to change during multi-pulse processing [23].

In parallel, substrate modification during pulse accumulation alongside laser processing modifies the optical surface properties resulting in decreasing ablation thresholds denoted as incubation [24], [25]. Incubation itself describes a sum-up of different effects involving the alteration of surface topography and chemistry as well as the disruption of internal order by defect-formation inside the substrate that altogether result in increasing laser absorption. To which extend the individual laser-induced substrate modifications contribute to incubation might differ significantly depending on the material and the laser parameters used. Incubation has not been considered in DLIP-processing so far. Especially in USP-DLIP, where pattern formation involves precise tailoring of threshold-related material response [16], the reduction of effective ablation thresholds in direct relation to the overlapping pulse count might considerably affect the resulting pattern morphologies.

In this work, multi-pulse effects on pattern formation during USP-DLIP processing are investigated for Cu using femtosecond laser pulses and a near-infrared wavelength, exhibiting a pronounced incubation behavior in previous studies [26],[27]. To monitor the individual impacts of surface chemistry and topography modification as well as defect implantation on overall incubation, a complementary multi-method approach is applied including confocal laser and scanning electron microscopy, electron back-scatter diffraction, UV–Vis spectroscopy, statistic image segmentation and numerical analysis. To include parametrization related influences into the investigation, altering DLIP setups as well as an application relevant fluence spectrum spanning the different ablation regimes observed on USP processed Cu are applied in the experiments. The combined evaluation of the different examination methods in mutual complementation allows for the determination of the individual USP-DLIP specific incubation mechanisms and their effect on pulse-wise primary and sub-pattern formation during multi-pulse processing. Following this approach, our investigation shed light on the predominant incubation mechanisms as well as their interplay in multi-pulse USP-DLIP of Cu and how they can be purposefully applied in targeted process parameterization.

2. Materials and methods

2.1. Material preparations and USP-DLIP

Sheets of cold rolled oxygen-free Cu (>99.95% purity, thickness 1 mm, *Wieland*, Germany) were cut into coupons of 10 × 25 mm size. Fine grinding on 1200 Grid Silicon Carbide paper followed by three polishing steps (6 µm, 3 µm, 1 µm suspension with reducing pressure of 15 to 10 N) results in a mirror finish with a roughness $R_a < 10$ nm of the Cu samples. Mechanical preparation is followed by thorough cleaning with distilled water and ethanol to remove suspension remnants. To investigate the influence of microstructure on laser-material interaction during the experiments, one batch of samples underwent annealing for 12 h at 450 °C and 10^{-7} mbar in a vacuum furnace. Said samples underwent electropolishing to avoid mechanical surface deformations, as described in [28].

Cu develops a native oxidation layer of Cu_2O and CuO by atmospheric storage, whereas process related agglomeration of oxidic redepositions also occurs during USP-DLIP [29]. Low concentrations of citric acid have been shown to remove both types of oxide [29],[30] and are therefore used to assess the influence of oxidation layers on optic surface properties. Deoxidized samples are produced by immersion in 3% citric acid for one minute in an ultrasonic bath directly before USP-DLIP processing or characterization.

USP-DLIP was conducted using a *Ti:Sapphire* laser source emitting ultrashort laser pulses with a pulse duration t_p of 100 fs at Full Width Half Maximum (FWHM) and a centered wavelength λ of 800 nm. An optical setup primarily containing a wave plate, diffractive optical element (DOE) and multi-lens system allows for the formation of two-beam interference patterns in µm and sub-µm scale on the sample surface [16]. While the wave plate is adjusted to alter the orientation of linear beam polarization in relation to the inference pattern to either s- or p-polarization, the setup of both DOE and multi-lens system defines the pattern periodicity P by adjusting the single beam incidence angle Θ according to Eq. (1).

$$p = \frac{\lambda}{2\ sin(\theta)} \tag{1}$$

In the experiments, pattern periodicity was varied between 6 µm, 3 µm and 750 nm. Cu surfaces were either processed by multi-pulse overlaps of $N = 1$, 2, 5 and 10 pulses on a single spot or planar patterning by scanning the sample surface in continuous pulsing mode at a pulse frequency of 1 kHz. In the latter case, pulse overlap is controlled by adjusting the x- and y- hatching distances in relation to the laser spot diameter of 70 µm. The applied fluences ranged from 0.31 J/cm^2 to 4.0 J/cm^2 partly including the low to the middle-fluence processing regime of Cu [31]. Fluences denoted in the results section are corresponding to the mean fluence at Full Width Half Maximum (FWHM) of the interference modulation, which has been calculated applying the mentioned spot diameter and pulse frequency as well as the measured seed beam power and 22.2% power loss of the optical system.

2.2. Characterization

2.2.1. Confocal laser scanning and scanning electron microscopy (LSM, SEM)

Characterization of the alteration in surface topography by USP-DLIP was conducted by means of confocal laser scanning microscopy (LSM) utilizing a *LEXT OLS4100 3D Measuring Laser Microscope* by *Olympus* (50× lens, 2× and 6× increased magnification, laser wavelength 405 nm) and scanning electron microscopy (SEM) (*Helios Nanolab600* by *FEI* and *Helios PFIB G4 CXe* by *Thermo Fisher*). Six individual samplings have been conducted for topographic characterization in relation to individual USP-DLIP parameters to include statistical dispersion. High resolution SEM imaging and characterization involved both secondary and back-scatter electron contrast (SE, BSE) combined with electron back-scatter diffraction (EBSD). High-resolution SE imaging was performed in immersion mode using the in-lens detector, while BSE imaging utilized a single segment retractable solid-state detector to visualize the grain orientations and surface topography of the sample. In both cases, an acceleration voltage of 5 kV was used, while in SE imaging, a beam current of 86 pA and in BSE imaging a beam current of 1.4 nA was applied. SEM imaging in SE contrast additionally involved a sample tilt of 52° degree to improve the visualization of topographical features. EBSD measurements were carried out using a high-speed CMOS camera (*Velocity Super* by *EDAX*) at 20 kV acceleration voltage and a beam current of 26 nA. The step size on a hexagonal grid was set to 250 nm. Lattice planes parallel to the sample surface of selected grains were

extracted using *OIM Analysis 8.6* software by *EDAX* in order to correlate their response to the laser irradiation.

2.2.2. UV–Vis spectroscopy

A *PerkinElmer Lambda 750* UV–Vis spectrometer was used to determine the optical absorptance of the differently prepared initial state Cu surfaces as well as absorptance increase due to pulse agglomeration alongside USP-DLIP processing. The measurement was performed for electro-magnetic wavelengths of 800 to 200 nm (1.55 to 6.2 eV) with 1 nm increments and 0.2 s integration time utilizing a 100 mm InGaAs integration sphere to guide the non-absorbed part of probing radiation to the detector. Due to the optical beam path involving several gratings and mirrors, the probing beam polarization is altered from circular to partly linear before it irradiates the samples. This feature is purposefully used in this study to allow for a qualitative assertion of polarization and topographic effects during multi-pulse processing by measuring the line-like patterned surfaces both in s- and p-polarization orientation to the probing beam. Multi-pulse agglomeration effects on absorptance have been monitored after irradiation with 1, 2, 5 and 10 pulse overlaps at a fluence of 2.1 J/cm^2 and 3 µm pattern geometry.

2.2.3. Numerical analysis

Material processing using ultrashort laser pulse durations in the femtosecond regime involves complex physical laser-material interactions like e.g. multi-photon absorption in dielectrics and ceramics as well as considerable thermal non-equilibria between the electron and lattice sub-systems in metals. These different physical interactions altogether result in ablation dominated material response closely linked to fluence levels surpassing the material specific ablation threshold F_{abl}, allowing to precisely tailor surface feature sizes down to the sub-µm scale. In case of USP-DLIP, this relation can be utilized to define the targeted width of the ablated area in order to design primary pattern geometries as illustrated in Fig. 1a [16]. However, in case of multi-pulse surface processing the optical properties of the substrate surface change due to incubation leading to a reduction of F_{abl} that has to be considered in process parametrization, which is especially the case for Cu [32].

Alongside the previously described characterization methods, numerical analysis of the thermal response of Cu surfaces to USP-DLIP irradiation was therefore utilized to further assess the different accumulation effects on line-like primary pattern formation that contribute to incubation in multi-pulse processing. The 2D two-temperature model (TTM) for USP-DLIP irradiation of Cu surfaces previously introduced in [16] was modified to include single beam polarization as well as pulse-wise increase of surface absorptance during multi-pulse processing. The key influences of altering laser-material interaction are fully described by the thermal heat source term S in the TTM denoted by Eq. (2),

$$S(\mathrm{x,z,t}) = \alpha A_x \frac{I(x)}{\sigma\sqrt{2\pi}} exp\left[-\frac{(t-t_0)^2}{2\sigma^2} - \alpha z\right] \tag{2}$$

which involves the energy absorption correlating to the Beer-Lambert Law, where α is the absorption coefficient and A_x the localized optical absorptance. The spatial distribution of laser intensity correlating to the interference pattern is denoted by $I(x)$ while the temporal distribution of laser power in relation to the arrival time t_0 of the pulse at maximal intensity is defined by the standard deviation σ involving the pulse duration t_p:

$$\sigma = \frac{t_p}{2\sqrt{2ln2}} \tag{3}$$

Optical absorptance of Cu surfaces varies depending on initial surface condition as well as multi-pulse agglomeration. Hence, the energy absorption in S is modelled to enable the inclusion of experimental values from UV–Vis spectroscopy. Here, absorptance A_0 at different states of pulse agglomeration during surface processing is taken as the mean value between s- and p-pol from UV–Vis data for $N = 1, 2, 5$ and 10 at a wavelength of 800 nm (1.55 eV). The increase of energy absorption alongside ultrashort pulsed irradiation due to thermally enhanced electron excitation states ΔeV [33] is involved for both A_0 and α in the numerical calculation of the TTM by approximating $\Delta T_e \sim \Delta eV/k_B$, where T_e is the electron temperature and k_B the Boltzmann constant. This approach introduced in an earlier study shows good correlation to referenced experiments [33],[34].

Since optical absorptance of USP irradiation alters with incidence angle between s- and p-pol [36], the topographic influence on optical absorptance during multi-pulse pattern formation was additionally involved. Localized absorptance A_x involves the alteration of irradiation incidence angle Θ_x perpendicular to the line-like surface pattern. The ablation area geometry of the primary surface pattern is approximated as a circular segment as illustrated in Fig. 1b where the slope of Θ_x can be determined by Eq. (4) using the individual ablation width w and depth d from topographic characterization.

$$\theta_x = arcsin\left(x\frac{8d}{4d2 + w2}\right) \tag{4}$$

The polarization dependent absorptance $A_{s,p}$ in response to surface topography can be determined as (1-$R_{s,p}$) either for s- or p-polarization by calculating the Fresnel equations for R_s or R_p in relation to Θ_x utilizing the optical properties of Cu from literature data [35]. To enable the determination of overall localized absorptance A_x including topographic absorption modelling, UV–Vis data and electron excitation in numerical analyzation, the calculated literature values for $A_{s,p}$ are approximated by

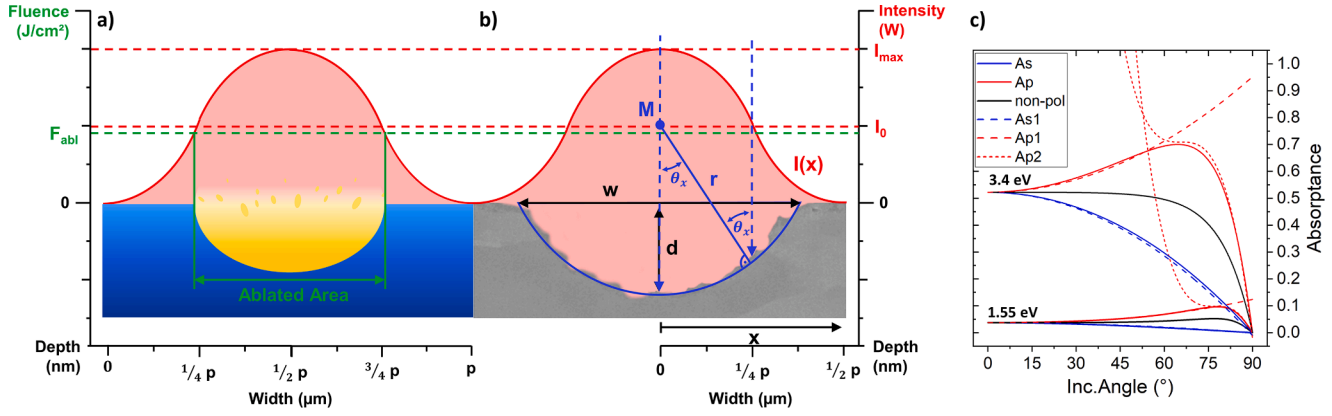

Fig. 1. Schematic illustration of a) the relation between interference intensity pattern, ablation threshold F_{abl} and laser-material interaction and b) the influence of surface inclination to the localized irradiation incidence angle Θ_x due to advanced material ablation below the intensity maxima. c) alteration of optical absorptance for 1.55 eV and 3.4 eV in relation to beam polarization and incidence angle calculated from literature values (A_s, A_p, *non-pol*) [35] and approximated (A_{s1}, A_{p1}, A_{p2}).

a set of equations relating to $A_0(\Delta T_e)$ and $\Theta_x(x,w,d)$, as well as the pseudo-Brewster angle BA for Cu corresponding to A_0. Depending on beam polarization, A_x is either represented by A_s or A_{p1} (for $A_{p1} < A_{p2}$) | A_{p2} (for $A_{p1} > A_{p2}$).

$$A_x \begin{cases} A_s = A_0\left(1 - \theta_x^2 \bullet 10^{-3.9}\right) & (5) \\ A_{p1} = A_0 + \theta_x^{(2.53-A_0)}\left(\dfrac{A_0 \bullet 10^{-3}}{-45 \bullet A_0 + 33.7}\right) & (6) \\ A_{p2} = (1.3 \bullet A_0 + 0.05) - 5(\theta_x - (A_0 + BA - 2))3 \bullet 10^{-5} & (7) \end{cases}$$

The comparison between polarization dependent absorptance $A_{s,p}$ calculated by eqs. (5–7) and literature values in relation to Θ_x is illustrated in Fig. 1c for A_0 at 1.55 eV and 3.4 eV showing a high level of conformity.

Aside of absorptance alteration in response to topography, beam polarization also influences intensity modulation in laser interference, which was shown to have a significant effect on pattern formation [37]. In case of two-beam interference, the modulation of intensity $I(x)$ in relation to the electrical field amplitudes E_1 and E_2 and incidence angle Θ of the individual partial beams is described by Eqs. (8) and (9) for either s- or p-polarization.

$$\text{S} - \text{polarization}: \quad I_s(x) = \frac{1}{2}\left(E_1^2 + E_2^2\right) + E_1E_2 \bullet cos\left(\frac{4\pi}{\lambda}sin(\theta)x\right) \tag{8}$$

$$\text{P} - \text{polarization}: \quad I_p(x) = \frac{1}{2}\left(E_1^2 + E_2^2\right) + E_1E_2cos(2\theta)cos\left(\frac{4\pi}{\lambda}sin(\theta)x\right) \tag{9}$$

Assuming equal distribution of initial laser intensity I_0 between both partial beams with $I_1 = I_2 = \frac{1}{2}I_0$ and $E_1 = E_2 = \sqrt{\frac{I_0}{K}}$, where $K = 1$ is approximated, Eqs. (8) and (9) can be transformed to:

$$I_s(x) = I_0 + I_0 \bullet cos\left(\frac{4\pi}{\lambda}sin(\theta)x\right) \tag{10}$$

$$I_p(x) = I_0 + I_0 \bullet cos(2\theta)cos\left(\frac{4\pi}{\lambda}sin(\theta)x\right) \tag{11}$$

Replacing F_0 for I_0 and $w/2$ for x, where w corresponds to the ablation width, either the effective ablation threshold F_{abl} can be calculated from experimental data or the estimated ablation width for predefined F_{abl} can be determined involving polarization dependent pattern modulation.

$$F_{abl\,s} = F_0 + F_0 \bullet cos\left(\frac{4\pi}{\lambda}sin(\theta)\frac{w}{2}\right) \tag{12}$$

$$F_{abl\,p} = F_0 + F_0 \bullet cos(2\theta)cos\left(\frac{4\pi}{\lambda}sin(\theta)\frac{w}{2}\right) \tag{13}$$

Numerical analyzation of the thermal substrate response on USP-DLIP during multi-pulse processing was conducted by solving the TTM in a 2D depth profile utilizing the simulation software *FlexPDE*, where initial A_o, A_x and $I(x)$ are modified corresponding to pulse count N and beam polarization. Lattice heating corresponding to phase changes and material ablation is calculated at thermal relaxation τ_{eq} between the electron and lattice sub-systems of the TTM, where isothermal frontiers of the threshold temperatures for solid/liquid and liquid/vapor phase transitions mark the phase fronts.

2.2.4. Morphologic segmentation

Alterations in sub-pattern formation and geometry during multi-pulse processing via USP-DLIP have been monitored using the *MorphoLibJ* Plugin [38] of *ImageJ* (*FiJi*) [39] for the segmentation and morphological characterization of individual particles. In order to enable a targeted segmentation distinguishing between the individual crater-like sub-pattern features (in the following: craters), SEM images were taken in SE mode with increased topographic contrast allowing to separate the individual craters via watershed boundary conditions. Segmentation fragments are filtered out by size and shape filters (minimal particle size and aspect ratio) whereas each segmentation result was carefully monitored for left-over fragments or falsely filtered craters. Using the morphologic segmentation, the alterations in size, shape and orientation of the crater-like features in response to multi-pulse agglomeration were statistically evaluated to quantify the effect of beam polarization, laser fluence and pattern scale on the development of sub-pattern geometry during USP-DLIP processing within the first ten consecutive laser pulses.

3. Results and discussion

3.1. Effect of incubation on multi-pulse USP-DLIP

3.1.1. Pattern formation in response to periodicity

To investigate a possible effect of pattern scale on multi-pulse USP-DLIP processing of Cu surfaces, the three different periodicities 6 µm, 3 µm and 750 nm have been applied in multi-pulse overlaps of $N = 1$, 2, 5 and 10 on a single spot. The pattern geometry in terms of peak/valley surface ratio has previously been shown to be directly linked to the ablated area defined by the material specific ablation threshold F_{abl} in response to the fluence utilized, as visible in Fig. 1a. Here, the effect of incubation during multi-pulse processing must be included, which might vary significantly depending on the material processed and the laser parameters used. To investigate a broader range of laser/material interaction involving both spallative and phase explosion ablation, fluences for USP-DLIP have been chosen in both the low-fluence regime below 1.5 J/cm^2 and the mid-fluence regime ranging between 1.5 and 4 J/cm^2, where femtosecond pulsed ablation for Cu shows the highest efficiency according to Schille et al. [31]. This also fits to the $F_{max} = 7.4$ F_{abl} referenced in [25] taking the $N = 10$ and $N = 100$ multi-pulse ablation thresholds of 0.581 J/cm^2 and 0.307 J/cm^2 measured by Kirkwood et al. [26] into account. In a previous study, low-fluence USP-DLIP exhibited an ablation behavior mainly involving thermomechanical spallation, while in the mid-fluence regime photothermal phase explosion could be traced back as the dominant ablation mechanism after the second consecutive laser pulse [16].

In terms of localized laser/material interaction in response to the DLIP intensity pattern, the modulation depth induced by laser interference has to be considered, which decreases in case of p-polarization with enhancing incidence angle Θ [37]. In Fig. 2a, the sinusoidal intensity modulation for either s- or p-polarized two-beam interference calculated by Eqs. (10) and (11) is plotted for the pattern periodicities 6 µm, 3 µm and 750 nm. While the modulation depth for p-polarized (p-pol) interference does not alter significantly for both µm-scaled patterns of 6 µm ($I_0 \pm 99.2\%$) and 3 µm ($I_0 \pm 96.4\%$), a considerable difference occurs for high incidence angles as used for 750 nm pattern periodicity with a low intensity pattern contrast ($I_0 \pm 43{,}2\%$). Consequently, varying beam polarization can already be considered to influence pattern formation during multi-pulse USP-DLIP processing of Cu from interference modulation alone. In fact, a more pronounced increase of ablation area during consecutive pulsing is visible comparing both SEM images and the fluence dependent ablation plots in Fig. 2b, c and d in case of p-pol, which applies to a different extent on the individual pattern scales.

In 6 µm USP-DLIP processing, the difference between s- and p-polarized ablation width mainly becomes prominent in the low-fluence regime after a pulse count of five (see Fig. 2b). Here, p-pol ablation width surpasses the range, which would be estimated by applying the $N = 10$ ablation threshold from [26], while s-pol ablation width continuously stays below that threshold. Entering the mid-fluence regime, the slope of ablation width tends to drop with increasing pulse count N after

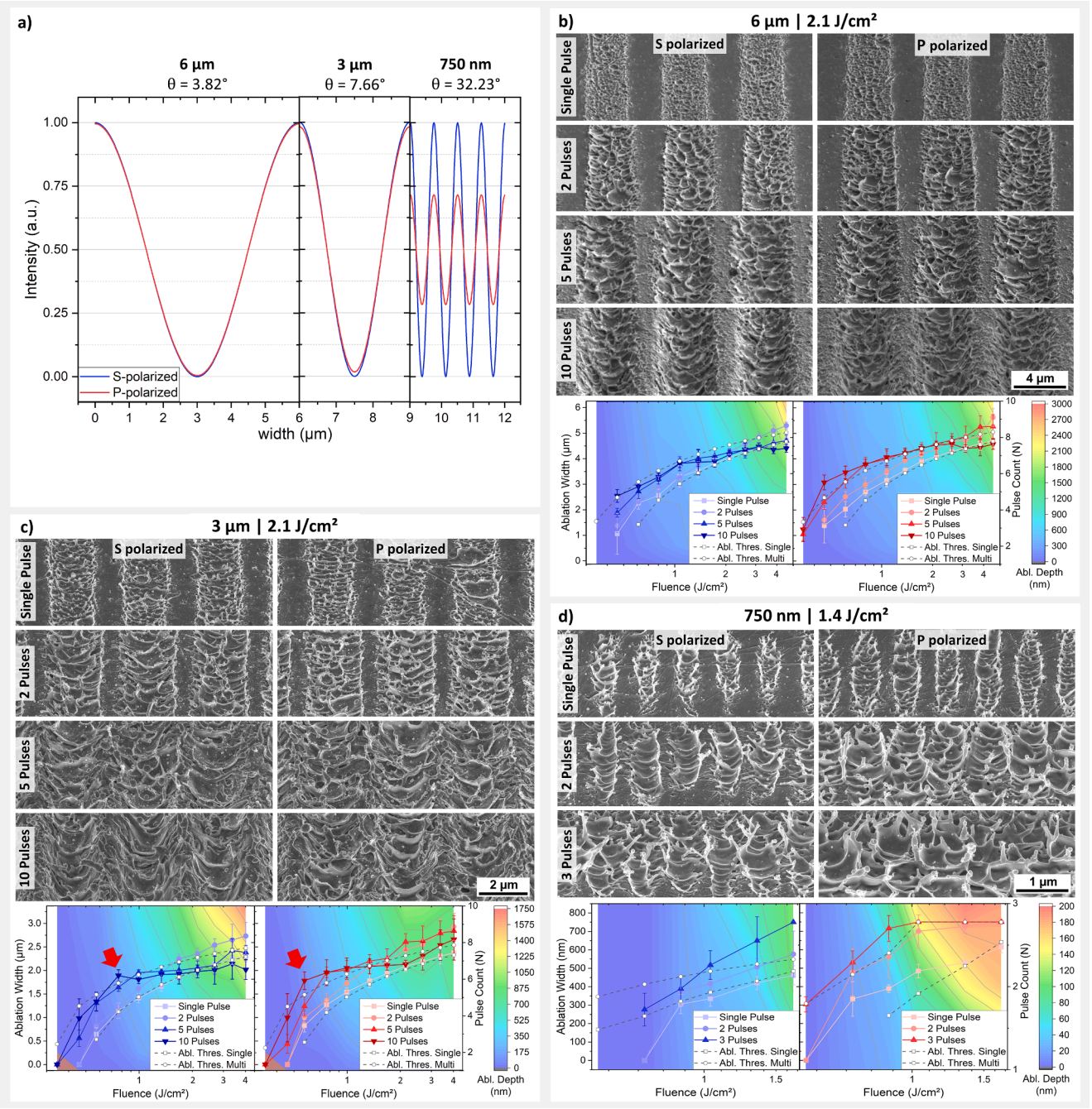

Fig. 2. Line-like USP-DLIP processing of the pattern periodicities 6 µm, 3 µm and 750 nm on Cu involving interference pattern modulation by altering linear single-beam polarization. a) Difference in two-beam interference pattern modulation between s- and p-polarization for each periodicity. b) SEM-imaging of 6 µm patterns applied by increasing multi-pulse overlap at 2.1 J/cm^2 for either s- or p-polarization followed by a combined plot of ablation width (line graph) vs ablation depth (underlaying heat map). c) SEM-imaging of 3 µm patterns applied by increasing multi-pulse overlap at 2.1 J/cm^2 for either s- or p-polarization followed by a combined plot of ablation width (line graph) vs ablation depth (underlaying heat map). The red arrows mark the individual setting points for s- and p-pol, where ablation area expansion is restricted for further increasing fluence and pulse-count. d) SEM-imaging of 750 nm patterns applied by increasing multi-pulse overlap at 1.4 J/cm^2 for either s- or p-polarization followed by a combined plot of ablation width (line graph) vs ablation depth (underlaying heat map). The ablation thresholds marked in b), c) and d) are corresponding to the single and $N = 10$ pulse ablation threshold of 1.06 J/cm^2 (Single) and 0.581 J/cm^2 (Multi) from [26] calculated by Eqs. (12) and (13). SEM images have been taken at a sample tilt of 52°. (For interpretation of the references to colour in this figure legend, the reader is referred to the web version of this article.)

a strong increase for the second pulse. This trend is more pronounced for s-pol pattern formation where this trend already involves $N = 5$. For both polarization orientations a pulse count of $N = 10$ exhibits a kink at 3.13 J/cm^2 (s-pol) and 2.68 J/cm^2 (p-pol), where a developed state of topographic pattern formation might get involved with laser/material interaction. In contrast to the ablation width ratio between the USP-DLIP patterns generated with different beam-polarization, s-pol processing induces a greater pattern depth than p-pol at similar fluence and pulse count, especially in the mid-fluence regime.

In case of 3 µm pattern periodicity, the previously observed kink in ablation width increase for higher pulse counts during multi-pulse processing can already be observed in the low-fluence regime at 0.76

J/cm^2 (s-pol) and 0.57 J/cm^2 (p-pol), as highlighted in Fig. 2c. For s-pol this point marks the onset of a plateau-like slope exhibiting constant ablation width for increasing fluences at both $N = 5$ and $N = 10$ pulse counts, which also continues into the mid-fluence regime. A difference between low- and mid-fluence regime s-pol ablation width is only visible for dual pulse irradiation, where the referenced $N = 10$ multi-pulse ablation threshold is increasingly surpassed. In contrast, the plateau-like slope of ablation width during multi-pulse p-pol processing can only be exhibited for $N = 10$ in the low-fluence regime, although it remains below the values for $N = 5$ from this point on. In parallel to s-pol, p-pol dual pulse ablation width also exceeds the range denoted by the referenced multi-pulse ablation threshold in the mid-fluence regime. Including the findings in [16], the second consecutive pulse applied in the mid-fluence regime induces a growing proportion of phase explosion in ablation, which leads to increasing melt-agitation and hence additional pressure mediated expansion of the ablation area. The observed stagnation up to reduction of the ablation area width with elevated pulse count suggests an effect of the pattern topography on laser/material interaction during multi-pulse USP-DLIP processing of 3 µm patterns, which considerably depends on beam polarization. Similar to the observations at 6 µm pattern periodicity, s-pol ablation depth surpasses the values of p-pol but on a significantly higher scale. The maximum s-pol ablation depth of 1.71 µm after 10 pulses at 4.02 J/cm^2 is almost double as high as the p-pol ablation depth of 0.88 µm with the same parameters. It is noteworthy that the actual maximum ablation depth of 0.99 µm for p-polarization was measured at a lower fluence of 2.1 J/cm^2, instead. Directly comparing overall ablation depth between 6 µm and 3 µm periodicities shows a similar depth vs fluence and pulse count ratio for s-pol, while ablation depth on p-pol 3 µm patterns fall below the values of 6 µm with an additional decrease after 2.1 J/cm^2. This might be related to partial ablation of the 3 µm peak areas in the course of reduced multi-pulse F_{abl} due to the less modulated p-pol interference pattern, which points out a polarization and pattern scale specific threshold fluence to achieve high pattern aspect ratio and quality that lies lower than the general mid-fluence range in case of p-polarized USP-DLIP.

Comparing the SEM images of both 6 µm and 3 µm patterns after different pulse counts applied at a fluence of 2.1 J/cm^2 in Fig. 2b and c, a difference in sub-pattern formation originating from melt agitation during ablation can be observed. Where the ablation areas on 6 µm patterns remain separated and the peak surface and geometry indicate minor thermal affection, overlapping structures of resolidified melt cover the peak areas on 3 µm patterns, which appear to have been ejected from the neighboring topographic minima in the course of ablation. Agitated liquified substrate has been shown to expand from the ablation site up to a certain range before it resolidifies due to enhanced convective cooling in the process of material expulsion in relation to the amount of super-critical lattice heating and the parallel pile-up of internal pressure during femtosecond pulsed laser irradiation of Cu [40]. Measuring the fluence-dependent quantitative pulse-wise increase of ablation width for both periodicities, pattern valley expansion ranges in the same order of magnitude in the low-fluence regime and for $N < 5$ in the lower mid-fluence range, where ablation starts to be dominated by phase explosion [16]. Based on this ablation kinetics, agitated melt originating from the further expanding ablation areas appears to completely cover previously unimpaired pattern peaks in case of lower pattern periodicities after a certain fluence-dependent pulse count in the mid-fluence regime, with a potential impact on further laser/material interaction from surface modification.

A significant alteration of the previously observed polarization/ablation depth relation can be determined for a pattern periodicity of 750 nm. In contrast to µm-scaled pattern formation, p-pol pattern depths exceed the ones measured for s-pol processing up to two-fold. In parallel, p-pol ablation width exhibits a rapid increase, where an overlap of neighboring ablation areas can be observed within only three consecutive pulses at low fluences close to the referenced single pulse ablation threshold of 1.06 J/cm^2 [26]. It is noteworthy that for fluences in the mid-fluence regime, this overlap already happens after the second pulse, which fits to the effect of phase explosion on melt-agitation previously discussed for 3 µm pattern scale. In a previous work, higher fluences induced a melt-overlap already after the first pulse, where pattern stability could not be retained for two consecutive pulses highlighting the negative effect of mid-fluence processing in this pattern scale [16]. In close relation, the highest ablation depth is measured for 1.4 J/cm^2 right below the mid-fluence regime. As also visible in the SEM images in Fig. 2d, further irradiation after melt-overlap leads to the destruction of pattern integrity by the formation of a stoichiometric topography of a randomized sub-pattern originating from phase explosion ablation kinetics, which has already been reported for sub-µm USP-DLIP patterning in earlier works [16],[17]. Taking the polarization dependent interference modulation into account, the moderately decreased laser intensity within the p-pol interference pattern minima (approx. 0.8 J/cm^2 in case of 1.4 J/cm^2) might suffice to induce surface melting up to ablation already after a low pulse agglomeration due to incubation, while the reduced peak intensity should cause lower ablation in comparison to s-pol, in contrast. By this, the increased pattern depth of p-pol might result from beneficial melt kinetics, similar to previous works, where melt pile-ups during sub-µm USP-DLIP of highly conductive metals have been shown to be usable as an effective mechanism in the formation of line-like topography patterns [41],[42]. However, in direct comparison the p-pol ablation values exceed the ones measured for the more sharply defined s-pol patterns already after the first pulse, where melt-overlap is not observed in both cases. In addition to decreased ablation depth, s-pol ablation width tends to undercut the single and multi-pulse ablation threshold boundaries, especially for low fluences. In contrast, p-pol ablation width constantly surpasses single and multi-pulse ablation threshold and even shows ablation on lower fluences than s-pol, which is not consistent with the difference in interference pattern modulation indicating additional effects on sub-µm USP-DLIP processing.

In direct comparison, the investigated pattern periodicities can be divided relating to the effect of material specific ablation kinetics on pattern formation during multi-pulse USP-DLIP: 6 µm shows an almost linear relation between both ablation depth and width to both fluence and pulse count with low dependency on the fluence regime, where however p-pol seems to have a slightly higher effect on ablation width compared to the comparably low interference modulation. On 750 nm patterns, an increase of melt agitation from altering ablation kinetics due to incubation leads to melt pileups covering the peak areas especially in case of p-pol, where the topographic patterns are not stable for a higher number of overlapping pulses. In the case of 3 µm periodicity an intermediate behavior can be observed, where especially the formation of pattern geometry but also ablation related sub-patterns during multi-pulse processing can be divided by the involvement of either spallation or phase explosion. For mid-fluences on one hand, pattern peaks appear to be increasingly eroded during p-pol multi-pulse processing at fluences higher than 2.1 J/cm^2 as visible in the reducing pattern depth at $N = 10$, while they remain less affected aside of the visible melt overlap in case of s-pol. In the low-fluence range, a mostly parallel pattern formation behavior between s-pol and p-pol USP-DLIP can be observed suggesting a fluence/pulse count relation of pattern formation fitting closer to F_{abl} values from literature according to previously described incubation behavior of Cu [26]. Due to the intermixed relation between ablation kinetics and pattern formation, further investigation on the effect of incubation in multi-pulse USP-DLIP processing of Cu mainly focus on 3 µm pattern periodicity.

3.1.2. Pattern formation in response to altering ablation mechanism

In Fig. 3, topographies of 3 µm patterns generated by planar surface scanning with an absolute agglomeration of 21 ± 0.78 J/cm^2 are visualized by both SEM imaging and a comparison of the achieved topographic parameters. Between the individual patterns, the effect of s-pol versus p-pol USP-DLIP on pattern morphology is investigated using different fluences in the low- and mid-fluence regime at adjusted pulse

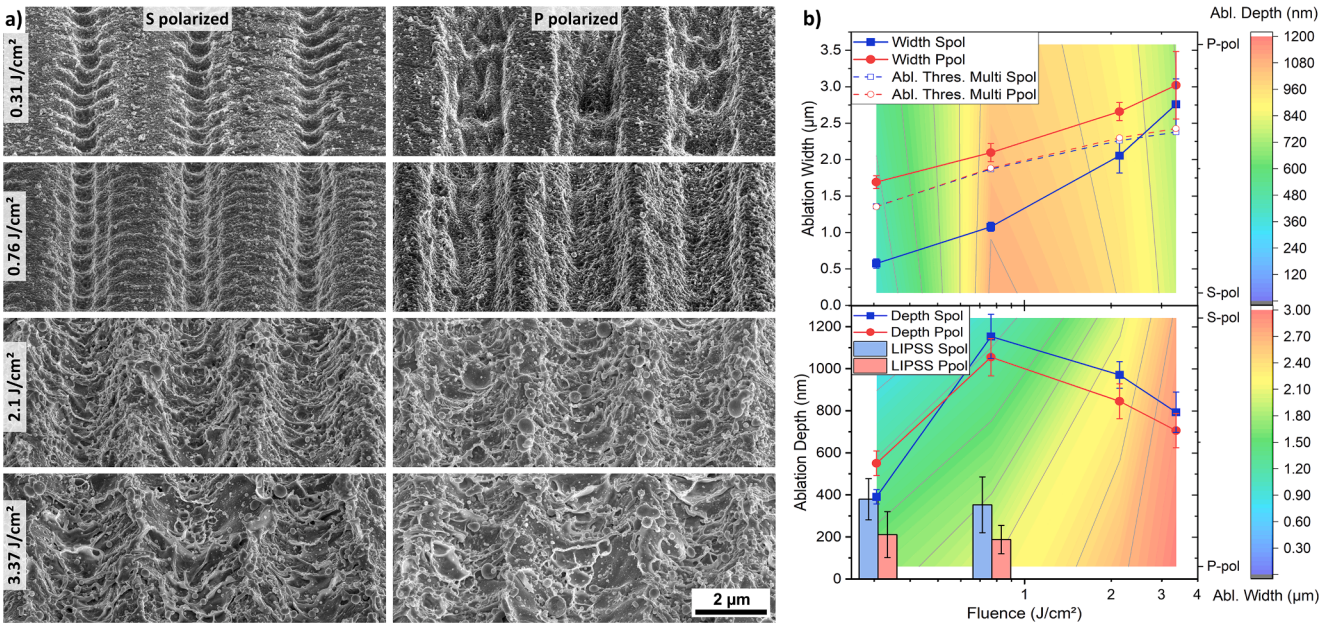

Fig. 3. a) SEM imagines and b) corresponding plotting of topographic parameters of line-like 3 µm patterns generated on Cu via USP-DLIP in planar scanning utilizing different fluences, x/y pulse overlaps and polarization parameters individually resulting in an agglomerated fluence of 21 ± 0.78 J/cm^2. The multi-pulse ablation thresholds in b) have been calculated applying $F_{abl}(N) = F_{abl}(1)N^{(S-1)}$ [24] with $S = 0.76$ [26] for both s- and p-pol interference pattern modulation. SEM images have been taken at a sample tilt of 52°.

overlap (0.31 J/cm^2, $N = 70$, scanning speed $\Delta x = 1$ mm/s | 0.76 J/cm^2, $N = 28$, $\Delta x = 2.5$ mm/s | 2.1 J/cm^2, $N = 10$, $\Delta x = 7$ mm/s | 3.37 J/cm^2, $N = 6$, $\Delta x = 11.5$ mm/s). A differentiation between low- and mid-fluence regime USP-DLIP can directly be applied comparing the individual sub-patterns, where the involvement of melt-agitation in pattern formation is clearly visible after mid-fluence processing and appears to be absent on low-fluence patterns. This can be linked back to the dominating ablation mechanisms in the different fluence regimes, where in case of low fluence thermomechanical spallation can be assumed, whereas phases explosion prevails at mid-fluence within the first two pulses. While the sub-pattern morphology seems to be independent of beam polarization in case of mid-fluence ablation, patterns generated by low-fluence irradiation differ significantly in both primary and sub-pattern formation between s- and p-polarization. Most obvious is the difference in the peak/valley ratio where ablation width is significantly higher on p-pol and increases to a much lower extend with further enhanced fluences compared to s-pol. Secondly, both fluences in the low-fluence regime exhibit LSFL formation in perpendicular orientation to the beam polarization adding to the difference between s-pol and p-pol patterns. Relating the measured ablation widths to the individual pulse count dependent ablation thresholds $F_{abl}(N)$ according to Jee et al. [24] (calculated by applying the incubation coefficient $S = 0.76$ provided in [26]) in Fig. 3b additionally points out the significant difference in multi-pulse ablation between s- and p-polarization via 3 µm USP-DLIP. Ablation width of p-pol patterns constantly surpass the estimated values with an additionally increasing ratio in the mid-fluence regime. In contrast, ablation width of s-pol patterns significantly undercuts the width corresponding to $F_{abl}(N)$ in the low-fluence regime until the measured values are approaching the ones of p-pol with increasing contribution of phase explosion ablation in the mid-fluence regime, where the ablation threshold estimated pattern width is finally surpassed for 3.37 /cm^2. Since intensity pattern modulation does not alter to that extend in case of $\Theta = 7.66°$ for 3 µm periodicity, topography-induced effects on absorptance for s- and p-polarization appear to be involved, here.

Ablation depth shows a steady increase with decreasing pulse-energy undergoing a sudden drop in the case of 0.31 J/cm^2. This behavior points out a reducing efficiency in the achievement of high pattern aspect ratio with accumulating fluence in direct relation to the extent of phase explosion in the mid-fluence regime, which appears to also affect s-pol in case of planar patterning in contrast to the previously shown behavior during single spot ablation. However, the overall polarization related dominance in either ablation width (p-pol) or depth (s-pol) development for µm-scaled pattern periodicities still applies, as visible in the comparison plots in Fig. 3b.

On low-fluence patterns, LSFL depth has been measured to allow for the evaluation of additional effects of LIPSS-formation that overlaps with the actual DLIP-patterning. Interestingly, LSFL depth is inverse to the measured ablation width for the different polarizations, suggesting a mutual influence between DLIP and LIPSS pattern, similar to recent findings [21]. If LSFL depth is subtracted, the corrected ablation depths of s- and p-pol at 0.76 /cm^2 are approx. on par with 2.1 J/cm^2, while overall formation of s-pol patterns at a fluence of 0.31 J/cm^2 appear to majorly dependent on the LSFL mechanism due to corresponding pattern and LSFL depths. The calculated multi-pulse ablation threshold equals to 0.38 J/cm^2 for this parametrization setup, which still undercuts the interference modulated peak fluence of approx. 0.61 J/cm^2 for both s- and p-pol, showing a significant overestimation of the incubation effect for s-pol USP-DLIP. Concurrently, the reduced energy absorption favors LSFL formation linked to sub-ablative threshold fluences on Cu [18] over ablative substrate interaction, probably leading to the different extent of LSFL depth between s-pol and p-pol. By this, the substrate response to 3 µm USP-DLIP with different polarization corresponds to the previously observed behavior for 750 nm, where s-pol ablation exhibited sub-threshold widths, while topographic patterning was achieved for sub-threshold fluences in case of p-pol, in contrast.

3.2. Impact of individual incubation effects during USP-DLIP

In the previously described topographic characterization, multi-pulse USP-DLIP pattern formation on Cu was shown to be influenced by incubation in differing response to both pattern scale and beam polarization in contrast to homogeneous incubation previously described for spot ablations utilizing gaussian intensity distribution [24],[26], [27]. This might be due to a differing individual impact of chemical, topographical and thermomechanical surface modification in case of

USP processing with an intensity distribution altered by DLIP, which will be further analyzed in the following sub-sections.

3.2.1. Overall incubation

The overall incubation during multi-pulse processing with 1, 2, 5 and 10 consecutive pulses utilizing a fluence of 2.1 J/cm^2 and 3 µm pattern periodicity was analyzed by measuring the alteration of optical absorptance via UV–Vis spectroscopy. The individual samples have been processed utilizing adjusted pulsing frequency and scanning speed to allow for spatially patterning at specified pulse accumulation (N = 1: 250 Hz, Δx = 17.5 mm/s | N = 2: 500 Hz, Δx = 17.5 mm/s | N = 5: 1 kHz, Δx = 14 mm/s | N = 10: 1 kHz, Δx = 7 mm/s). A partly linearly polarized probing beam allowed for the parallel qualitative investigation of the effect of polarization orientation in relation to the line-like pattern topography on overall surface absorptance. In Fig. 4a, a continuous enhancement of absorptance alongside increasing pulse count for the whole spectrum of probed wavelengths is apparent especially for N = 5 and N = 10 pulses in case of as-processed Cu surfaces (left graph of Fig. 4a). Tilting the orientation of beam polarization to the pattern geometry exhibits a minor total effect on overall absorptance with slightly higher values for p-pol, which additionally increases for higher pattern depths in case of N = 10 pulses in the Near IR spectrum. Since the probing beam was only partly linear polarized, this effect can be assumed to increase for fully linear polarized irradiation. For low pulse counts, the difference in absorptance between one and two consecutive pulses is minor and lies below the measured differences of s- and p-polarization at 800 nm, corresponding to the utilized laser wavelength. As soon as deoxidation via immersion etching in citric acid is applied, absorptance drops significantly exhibiting an increasing magnitude scaling with N (from N = 1 with approx. -16.8 ± 0.8% up to N = 10 with

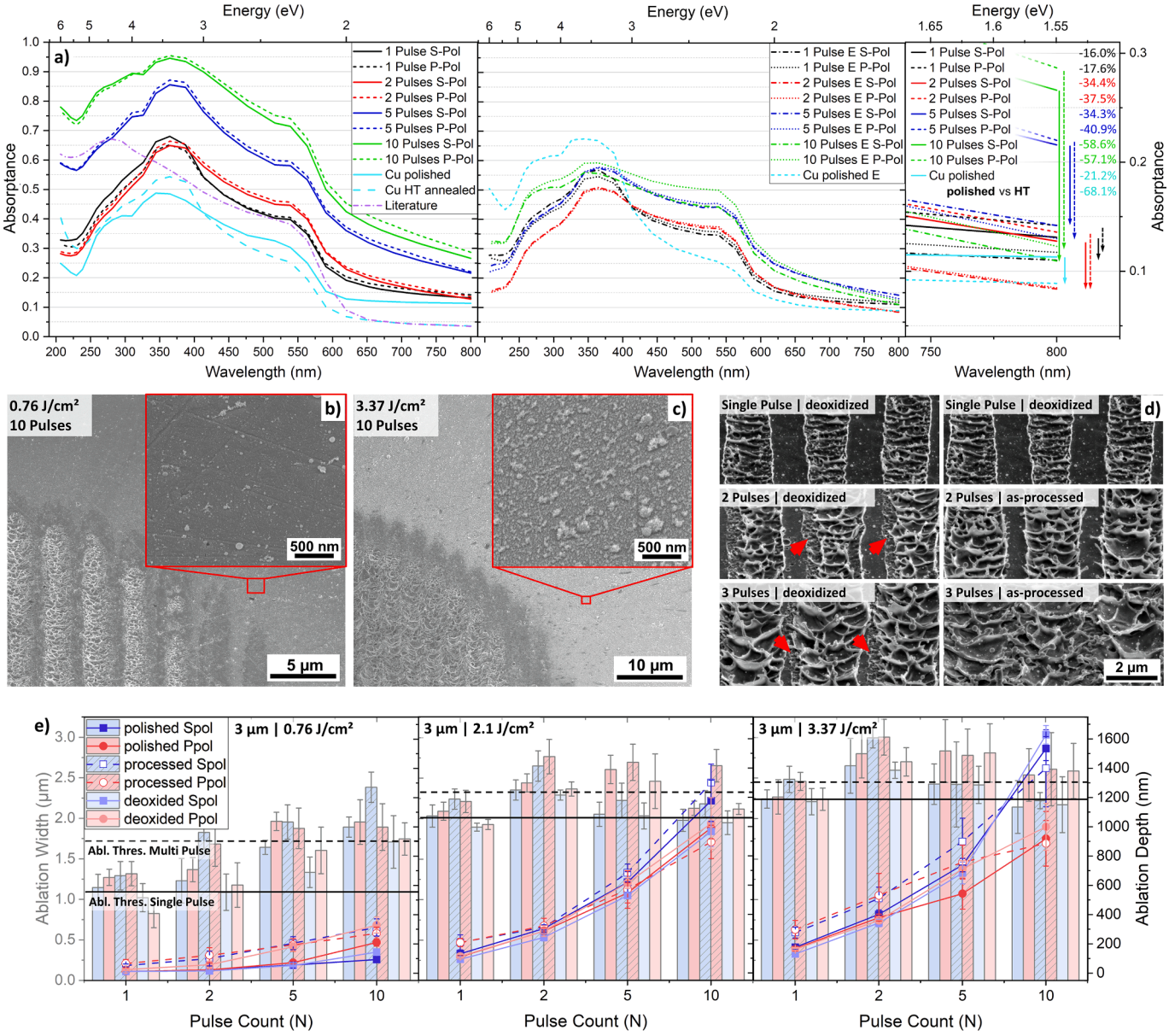

Fig. 4. Investigation of the effect of overall absorptance on USP-DLIP processing at a pattern periodicity of 3 µm. a) UV–Vis spectroscopy on USP-DLIP surfaces with a pulse overlap of N = 1, 2, 5 and 10, as well as polished and high temperature annealed Cu reference surfaces. Left graph: as-processed/−polished state. Middle graph: after immersion etching. Right graph: comparison between the optical absorptance at the laser wavelength of 800 nm. b) process-related redepositions after 10 pulses at 0.76 J/cm^2. c) process-related redepositions after 10 pulses at 3.37 J/cm^2. d) comparison of increasing ablation width/reducing ablation threshold at 2.1 J/cm^2 with and without intermediate deoxidation starting from deoxidized initial surface conditions. e) effect of initial surface state of either polished, as-processed and deoxidized on pattern geometry formation in the course of ten consecutive pulses. SEM images have been taken at a sample tilt of 52°.

approx. -57.9 ± 0.8%). By this, the difference in absorptance between increasing pulse counts gets significantly reduced, where in case of near-infrared wavelengths, the *N*-relation of absorptance is canceled out (see middle and right graph in Fig. 4a). The drop in absorptance indicates a dominant contribution of oxidic redepositions in overall increase of the surface absorptance. In the course of continuous ablation via USP laser processing, a fraction of the ablated material tends to redeposit on the substrate surface covering both already processed and non-processed surface areas. In a recent study, the redeposited matter related to USP-DLIP processing of Cu was determined to predominantly consist of Cu_2O with a smaller ratio of superficial CuO [29]. Both oxide phases exhibit semi-conducting properties with optical bandgaps ranging from 2.02 to 2.62 eV for Cu_2O and 1.2 to 1.9 eV for CuO depending on interstitial defect density [43]. Especially the bandgap of CuO is in close relation to the photon energies of the utilized laser wavelength while the Cu_2O bandgap facilitates two-photon absorption. By this, both oxide phases exhibit an increased absorptance in comparison to metallic Cu, hence impacting overall surface absorptance. An additional effect on both optical and thermal interaction might as well be induced by the nano-scaled morphology of the oxidic surface agglomerates exhibiting a high surface/volume ratio [29],[44],[45], where the single particle size of 10 up to 40 nm does not appear to change in the mid-fluence regime [46]. In fact, USP-DLIP ablation on thermally oxidized Cu substrates corresponding to [47] showed a significantly reduced single pulse ablation thresholds of approx. 0.12 J/cm^2.

Alongside USP-DLIP induced incubation, the comparably high initial absorptance of mechanically polished Cu surfaces in relation to literature data [35] has to be emphasized, which still ranges more than two-fold higher after immersion etching. Due to a negligible topographical influence on the mirror-polished surfaces, increased absorptance can predominantly be related to either chemistry + crystallographic defects for the as-polished sample and crystallographic defects alone after etching. It has been shown that the crystallography of Cu influences oxidic passivation layer formation, with a direct relation between grain boundary density and oxide thickness [48], by which the superficial mechanical deformation from polishing appears to cause a double effect on absorptance, both by crystallographic surface defects and increased oxide layer thickness. Consequently, the absorptance of reference samples, which have been annealed at high temperatures inducing excessive grain-growth (HT) exhibit a significantly closer relation to the literature values for ideal single crystal states. Comparable deviations of initial absorptance between differently pre-treated Cu surfaces have also been observed in previous studies [26],[27].

Since immersion etching solely causes the removal of surface oxide [29], the incubating effects of both modified topography and crystallographic defect formation during USP-DLIP remain active on the post-processed surfaces. Against this background, the inverted difference in absorptance between $N = 1$ and $N = 2$ before and after immersion etching exhibits different facets of incubation at the initial phase of multi-pulse USP-DLIP: Comparing the absorptance at both pulse counts after etching indicates a higher topography related absorptance-increase by the smaller scaled sub-pattern of $N = 1$ (compare Fig. 2c) for the utilized wavelength of 800 nm. Absorptance of $N = 2$ patterns matches mechanically polished Cu surfaces after etching, instead, indicating both a neglectable topographic influence of the $N = 2$ sub-pattern and similar defect related incubation. This suggests that additional defect implantation after the second consecutive laser pulse has not yet surpassed the crystallographic deformation of mechanical polishing. In addition, the more pronounced decrease in absorptance for $N = 2$ indicates significant oxidic agglomeration already after the second pulse, which might be linked to the alteration of ablative interaction from spallation to phase explosion [16]. Comparing the quantitative agglomeration of oxidic particles between spallative (Fig. 4b) and phase explosion ablation (Fig. 4c) in vicinity to the ablation site of single laser spots further underlines the reinforcing influence of the more eruptive ablation mechanism, fitting to literature data on fluence related ion-release [49]. The increase of absorptance related to $N = 5$ and $N = 10$ can mainly be linked to oxide agglomeration by comparison of the as-processed and etched values, as well, whereas enhancing sub-pattern perturbation, primary pattern geometry as well as defect formation seem to play a subordinate role in overall incubation on Cu according to UV–Vis examination with partly linear polarized probing beam.

3.2.2. Incubation effects of surface oxide

To further assess the pulse-to-pulse effect of oxide agglomeration on USP-DLIP incubation, a series of consecutive pulses at 2.1 J/cm^2 in p-polarization was overlapped on single spots starting from a deoxidized initial state of the Cu surface, where a part of the samples was etched while mounted between each consecutive pulse. Comparing pattern formation within the first three pulses in Fig. 4d with and without process-related oxide agglomeration reveal a reduced enhancement of ablation width on continuously deoxidized samples. Here, the ablation areas remain separated after three pulses in contrast to as-processed surfaces, while a lesser ablated outer region is visible. The latter indicates an intermixture of ablation mechanisms with spallation in the outer lower fluence and phase explosion in the central higher fluence area of the intensity pattern. Even though oxide agglomeration was removed, widening of the ablation area can be determined on both sample series due to melt-mobility aside of oxide-agglomeration, which is however still less expressed after deoxidation. It can be noted that melt-covering of the peak-areas already takes place after the third consecutive pulse in as-processed state traced back to enhanced melt-mobilization alongside more pronounced phase explosion ablation, which is also indicated by increasing crater size of the sub-pattern.

The predominant impact of surface oxidation on optical absorptance of Cu surfaces especially in the near-infrared regime might additionally be effective at the initial state of USP-DLIP processing, when pre-decoration of Cu surfaces with oxidic redepositions is considered before irradiation, as visible in Fig. 4b and c. Alteration of ablation behavior is therefore compared in relation to beam polarization and fluence after $N = 1$, 2, 5 and 10 pulse overlap on a single spot for the different initial states as-polished, deoxidized and processed. In the latter case, the ablation spot was localized in direct vicinity to previously applied surface patterns, which were processed at an accumulated fluence of 21 ± 0.78 J/cm^2 applying the same pulse fluence as used in the single spot investigation. A clear difference in ablation width between the three different initial surface states can be determined in both the low- and mid-fluence regime in Fig. 4e. Parallel comparison to estimated ablation width from single and $N = 10$ multi-pulse ablation thresholds emphasize an enhancing impact of initial oxide decoration with increased fluence, where the multi-pulse ablation threshold is reached after two pulses at low-fluence and even surpassed in the mid-fluence regime. Deoxidizing appears to reduce not only initial ablation width, but also ablation area expansion rate in case of 0.76 J/cm^2 indicating a reducing effect on overall incubation in the low-fluence regime. In both 2.1 J/cm^2 and 3.37 J/cm^2 multi-pulse processing, differences between the varying initial surface states become leveled after $N = 5$ showing the previously described variation between s-pol and p-pol patterns with only one outlier in case of 2.1 J/cm^2 at $N = 10$, in previously processed state. Here, higher melt-agitation with increasing expansion forces during phase explosion might play the predominant role in pattern formation with lesser dependency on the initial state of the Cu surface. The effect of this ablation mechanism in the mid-fluence regime is already visible after the second pulse where ablation width generally surpasses the multi pulse threshold mark. Ablation depth follows the same trend with higher values for pre-processed initial sample states that start to be dominated by polarization dependent effects after $N = 5$ in the mid-fluence regime, where at 2.1 J/cm^2 an inverse trend between s- and p-pol can be observed. In case of 3.37 J/cm^2, reduced initial ablation appears to be involved with higher ablation depths after $N = 10$ indicating an important effect of surface conditioning within the first consecutive pulses on further processing. In the case of low-fluence

regime ablation, preconditioning remains the dominant factor within the first 10 pulses, where however deoxidized p-pol appears to be particularly suitable for high ablation rates.

From these results an enhancing effect of surface oxide on absorptance that directly influences USP-DLIP pattern formation can be stated, which leads either to increased ablation efficiency in the low-fluence regime or tends to affect pattern aspect ratio and quality in the mid-fluence regime on Cu surfaces. Based on these observations, the varying results of planar patterning at accumulated 21 J/cm^2 illustrated in Fig. 3 can be assumed to be co-triggered by altering fluence-dependent response on process-related oxide agglomerations, which also affect initial surface absorptance.

3.2.3. Crystallographic defects

The comparison of the absorptance between mechanically polished Cu reference and USP-DLIP patterned surfaces after immersion etching in Fig. 4a points out a low impact of mechanical substrate alteration on incubation over the amount of already existing deformation from polishing. Defect formation from USP processing on Cu is mainly linked to thermomechanical substrate response on laser irradiation, which is getting more pronounced with decreasing pulse duration and increasing fluence [40]. In direct comparison between the two ablation regimes observed for Cu, increasing melt-kinetics during phase explosion aggravates a correct interpretation of effective ablation threshold in response to USP-DLIP pattern modulation at 3 μm pattern periodicity, while patterns achieved by spallation exhibit high ablation contrast (see Fig. 3a). Further investigation of the incubating effect of Cu crystallography and defect formation during USP-DLIP therefore focusses low-fluence regime thermomechanical spallative ablation at 0.31 J/cm^2. Single scan lines have been applied utilizing an accumulated fluence of approx. 9.9 J/cm^2 ($N = 32$ at $\Delta x = 2.2$ mm/s), where the corresponding calculated multi-pulse ablation threshold of 0.65 J/cm^2 ranges slightly above the peak values of the interference modulation. The initial crystallographic surface state of the Cu substrate condition was altered between the originally intrinsic cold rolled Cu sheet microstructure exhibiting a superficial deformation zone of approx. 500 nm depth from mechanical polishing [29] and a deformation free state by annealing the sample for 12 h in 450 °C under vacuum atmosphere at a pressure of 10^{-7} mbar followed by electro polishing. Deoxidation via immersion etching was additionally included, to compare the combined and single initial incubation effects of surface chemistry and crystallography.

The crystal orientation sensitive BSE contrast utilized for SEM imaging reveals the difference of both initial substrate states as visible in Fig. 5a and b, where the original substrate grain structure can hardly be distinguished on cold rolled mechanically polished Cu, while clear grain differentiation is possible on annealed samples. The mechanically pre-deformed surfaces exhibit localized ablation sites from USP-DLIP processing, however with less expression on deoxidized samples. Clear effects of differing beam polarization on overall ablation can be found in sub-pattern formation, where LSFL perpendicular to the polarization angle appear to contribute to localized ablation for both s-pol and p-pol. Aside of a more pronounced LSFL formation in case of s-pol, clear differences of ablation rate between s- and p-polarization cannot be determined unambiguously due to the unsteady ablation. Stripes of brightened contrast are framing ablation areas in the intensity maxima of the interference patterns that exhibit an identical width on all samples, which might be linked to laser surface cleaning. On annealed surfaces, ablation is considerably reduced in comparison to the pre-deformed substrate state and cannot be detected on deoxidized samples at all, which is finally fitting to the fluence/ablation threshold estimation for the chosen parameter setup from literature data [26]. Ablation on as-polished annealed surfaces appears to be related to crystal orientation with contrasting results for individual neighboring grains also exhibiting a more pronounced substrate interaction in the case of p-pol irradiation (see Fig. 5b).

Further investigation of this phenomenon was conducted tracing individual p-pol USP-DLIP scan lines utilizing a combination of BSE and EBSD analysis to link local crystal orientation to laser induced substrate interaction. Detected surface morphology ranged between three interaction regimes, where the measured width of the interaction area was used to calculate the locally effective threshold linked to that phenomenon by utilizing Eq. (13). Threshold values below 0.58 J/cm^2 did not induce ablation but rather rippling of the Cu surfaces (visible in the dark contrasted twins in Fig. 5b, s-pol and p-pol, as-polished), which appears to be related to HSFL formation considering both the small sub-pattern scale below $\lambda/2$ and orientation relative to the beam polarization [19], [20]. Since HSFL are mainly linked to melt-resolidification, they also might affect the crystal state of the substrate after sub-ablative irradiation in size scales below EBSD sensitivity [50],[51]. Above 0.56 J/cm^2 spallative ablation was induced on the entire interaction area, whereas crater morphology and ablation width increase with decreasing threshold (visible in the bright contrasted grains and twin in Fig. 5b, s-pol and p-pol, as-polished) also exhibiting first traces of LSFL formation. In the transition range, the rippled topography exhibits intermediate interaction characterized by widening HSFL morphology with incipient spallation in the central area highlighting a preconditioning incubation effect of the melt-induced surface reorganization. A mixture of non-ablative and transition range interaction can be detected for the majority of identified crystal orientations as visible in the orientation triangle in Fig. 5c, where corresponding interaction is marked by a heat map colour code ranging from blue to green. Ablative interaction is concentrated close to the {110} and {111} planes with significantly

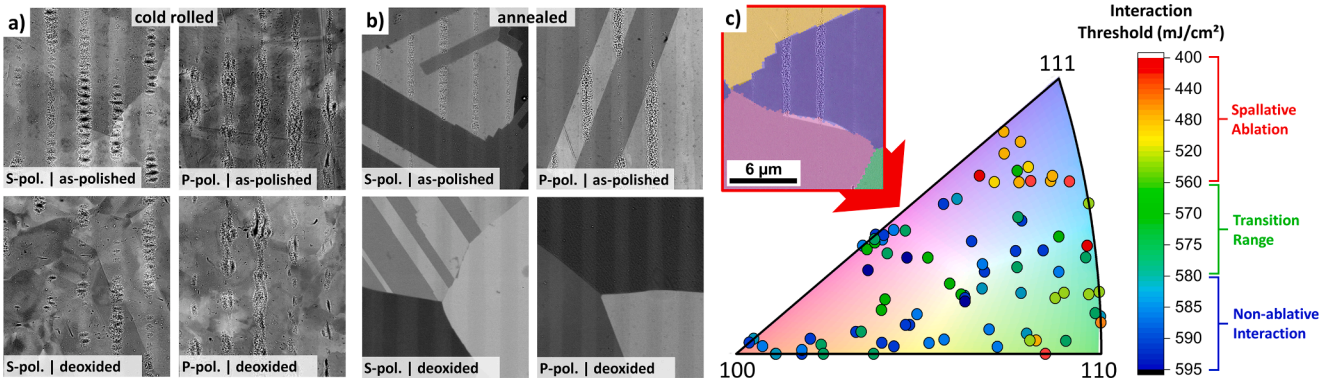

Fig. 5. Investigation of the effect of initial Cu crystallography on USP-DLIP ablation and incubation by single scan line patterning utilizing a fluence of 0.31 J/cm^2 and $N = 32$. a) SEM images in BE contrast of USP-DLIP patterns on mechanically pre-deformed Cu surfaces in as-polished and deoxidized state. b) SEM images in BSE contrast of USP-DLIP patterns on deformation free Cu surfaces in as-polished and deoxidized state. c) SEM analysis on annealed Cu samples utilizing BSE and EBSD in a complementary approach to link thermomechanical substrate interaction after USP-DLIP irradiation to local crystal orientation.

stronger expression of ablative behavior around {111}. According to this, thermomechanical defect implantation and agglomeration faces the lowest crystallographic resistance in ⟨111⟩ direction, corresponding to the early findings of Porteus et al. [52] who stated a comparably low threshold fluence for slip band formation on {111} oriented single crystal Cu mirrors in high power IR laser systems. Further increased ablation could be detected in the vicinity of grain boundaries. In more recent MD simulations on single crystal fcc Ni, {111} plane twinning was directly related to the formation of HSFL [51]. In another MD simulation study, single pulse USP irradiation of Cu showed altering thermal response in relation to crystal orientation as well, where melting and ablation depth is increased for {111} and {110} in comparison to {100} also involving a higher amount of defect formation in shape of voids and dislocations [53]. Here, the quantity of thermomechanical defect formation scales with {111} > {110} > > {100}, which fits the incubation gradient experimentally determined in this analysis. Crystallographic defects induce electron scattering, which affect surface plasmon formation and hence the reflection of laser irradiation, which is also highlighted by the observed increase in ablation interaction in the vicinity of grain boundaries. The physical course of surface modification however also involves HSFL formation as a preceding step before actual ablation, by which incubation by crystallographic defect implantation might involve nano-scaled surface roughening, as well [54].

3.2.4. *Topographic impact of primary pattern formation*

Alongside varying pulse accumulation and laser intensity, considerable topographic influences on absorptance corresponding to both primary and sub-pattern morphology in response to beam polarization have been apparent on USP-DLIP processed Cu in the previously described analysis. The effect of beam polarization on localized absorptance alongside topography modification on primary pattern formation was investigated numerically also applying FEM simulation of USP-DLIP induced substrate thermalization utilizing a specified 2D TTM.

Parallel to interference modulation, beam polarization influences localized absorption of radiation as soon as the incidence angle $\Theta \neq 0°$ [36],[44], which can either result from beam tilting on flat surfaces or by increasing topographic surface slopes. While the first case can be well

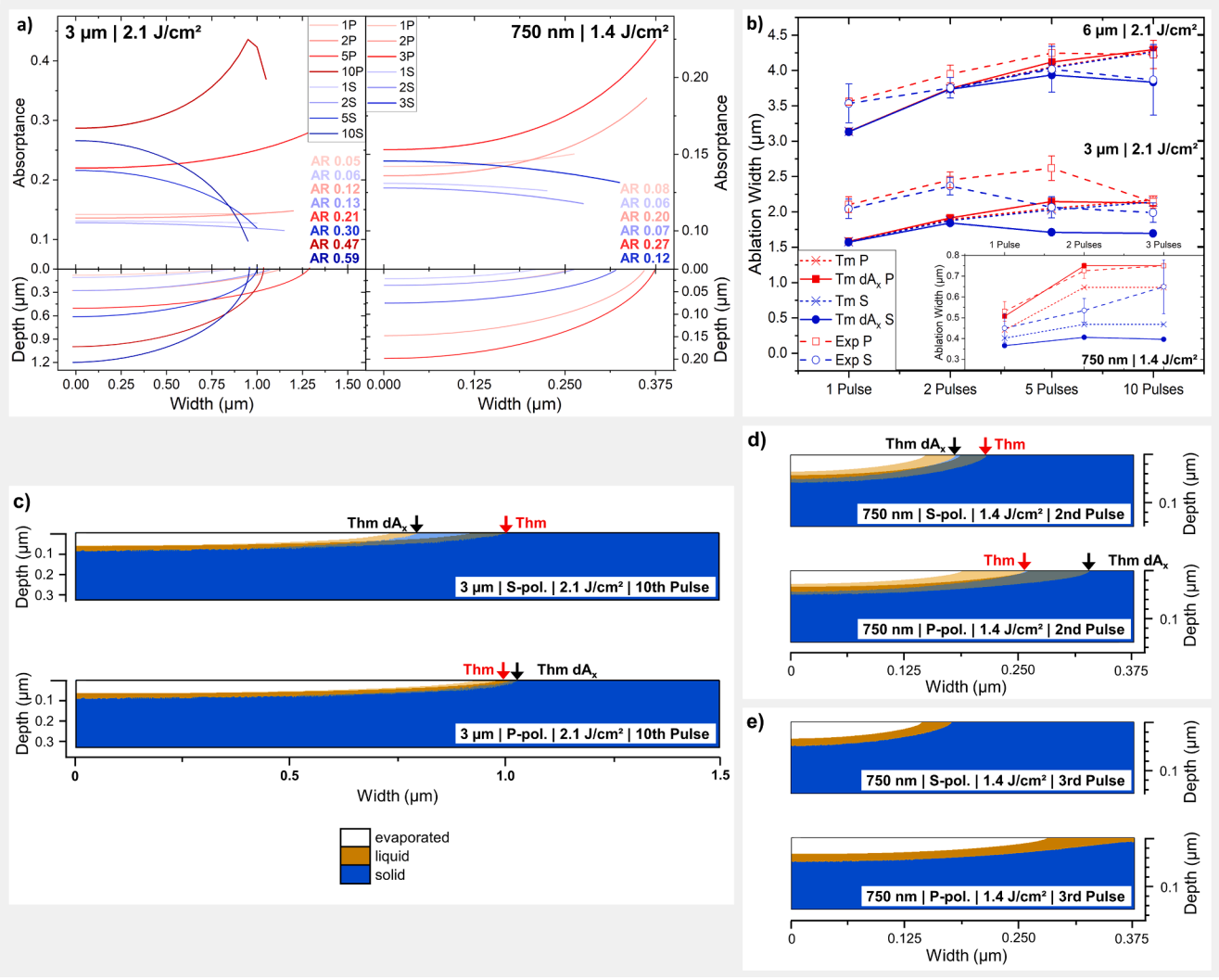

Fig. 6. Combined influence of topography development and beam polarization on multi-pulse USP-DLIP pattern formation with 6 µm and 3 µm at 2.1 J/cm^2 as well as 750 nm at 1.4 J/cm^2. a) localized alteration of absorptance in response to beam polarization and increasing pattern aspect ratio AR of USP-DLIP with 3 µm and 750 nm pattern periodicity. b) ablation width corresponding to substrate thermalization up to T_m calculated by numerical TTM simulation of USP-DLIP at 6 µm, 3 µm and 750 nm pattern periodicity and $N = 1$, 2, 5 and 10 with and without inclusion of topographically altered absorptance A_x in response to beam polarization. The calculated values are compared to experimental data. c) numerically calculated substrate thermalization corresponding to T_{hm} at τ_{eq} (=1.37 × T_m [55]) in response to USP-DLIP with s- and p-polarization of 3 µm periodicity at $N = 10$ with and without the inclusion of A_x. d) numerically calculated substrate thermalization corresponding to T_{hm} in response to USP-DLIP with s- and p-polarization of 3 µm periodicity at $N = 2$ and e) $N = 3$ with and without the inclusion of A_x.

described by the Fresnel equations, localized alteration of Θ_x in response to surface topography additionally requires full knowledge of mostly complex surface geometries. Taking advantage of the uni-directional periodic character of the line-like patterns, the local change in absorptance relative to Θ_x is characterized in direct correlation to the pulse-wise development of a single ablation site, which can be scaled up to the entire pattern. Utilizing the experimental data of fluence + pulse count specific ablation width and depth illustrated in Fig. 2, individual Θ_x slopes for intermediate processing steps can be calculated via Eq. (4). In Fig. 6a, the alteration of polarization dependent localized absorptance A_x correlating to increasing pulse counts is plotted in relation to the corresponding ablation area geometries for 3 µm and 750 nm at 2.1 J/cm^2 and 1.4 J/cm^2. A_0 at $\Theta = 0°$ is taken as a mean value from UV–Vis data for s-pol and p-pol of as-polished Cu at $\lambda = 800$ nm and $N = 1, 2, 5, 10$ in the as-processed state. Alongside a significant pulse wise increase of absorptance A_0 due to oxide agglomeration, an inverse trend of localized absorptance A_x is obvious between s-pol and p-pol. Beam polarization perpendicular to the line-like pattern induces further enhancing localized absorptance along the pattern slope in case of p-pol, while maximum localized absorptance can only be achieved in the ablation area center with decreasing gradient along the edge for s-pol. This polarization dependent absorptance modulation by altering surface topography determines the local uptake of the interference modulated laser intensity. By this, the actual substrate response involves the superposition of both the laser intensity and the absorptance modulation pattern. Consequently, ablation area width is shrinking for s-pol after $N > 2$ closely linked to the pronounced drop in absorptance, while it is increasing for p-pol along the further steepening slope of the ablation site. In the case of 3 µm, the increasing pattern aspect ratio finally induces incidence angles above the pseudo-Brewster angle for Cu at the outer edge of the ablation area at $N = 10$, where absorptance starts to drop for p-pol as well. Likewise, ablation area width starts to decrease similar to s-pol from this point on. The pseudo-Brewster angle for Cu ranges around 78.6° for 1.55 eV but tends to fall with increasing A_0 alongside incubation even below 70°. Applying Eq. (4), one can calculate an approximated pattern aspect ratio of 0.4, where localized absorptance tends to drop for p-pol, as visible for $N = 10$ with an aspect ratio of 0.47. Since aspect ratio/pulse count inversely scales with pattern size in case of USP-DLIP, the threshold aspect ratio for 6 µm is not achieved within $N = 10$, while on 750 nm patterns, aspect ratio does also not reach this critical value, however due to preliminary pattern disruption, in contrast.

For the sub-µm pattern scale, the slope in A_x increases stronger for p-pol in direct comparison to 3 µm, which can be related to the higher impact of melt-kinetics on primary pattern geometry already after two pulses. In the previously described topographic characterization, a significant deviation between estimated and measured ablation in relation to polarization specific intensity pattern modulation was apparent for 750 nm periodicity. Here, the modulated minimum fluence still ranging at approx. 56.8% of F_0 must be considered to interpret ablation area expansion alongside incubation and topographic absorption amplification of p-pol in comparison to s-pol USP-DLIP. However, the distinctive difference in ablation rate already apparent after the first pulse cannot be explained by the effects mentioned above, but rather indicates a preferential initial absorption of p-pol irradiation induced by the considerable partial beam incidence angle of $\Theta = 32.23°$ [36]. Involving a corresponding initial offset of Θ_x in the calculation of A_x induces differing absorptance between s-pol and p-pol even without topography involvement, which additionally increases with incubation (see Fig. 6a). This indicates that polarization specific initial absorption involved in USP-DLIP processing potentially counter balances the reduced fluence amplification by interference modulation in case of p-pol inducing ablation in inverse relation to the actual intensity pattern modulation between s- and p-pol at 750 nm periodicity. A similar but lesser pronounced polarization relation of initial ablation can also be exhibited for 3 µm and 6 µm pattern periodicity whereas this effect appears to still be valid with decreasing partial beam incidence angles.

Involving interference pattern modulation as well as chemically and topographically increased absorptance in numerical FEM simulation of the ultrafast substrate heating allows to identify the combined effects on substrate response in USP-DLIP. Since overall incubation was mainly related to oxidic agglomeration with an insignificant contribution of both defect formation and topography in the UV–Vis examination, the achieved spectroscopic data was utilized to model chemically related absorption increase. To allow differentiation between the single effects of interference modulation and topographic pattern formation alongside chemical incubation, numerical simulation has been conducted with and without inclusion of locally altered A_x. Due to lattice temperatures above the phase explosion threshold temperature T_{PE} [56] achieved in numerical simulation, ablation-kinetics can be considered to involve melt-agitation. Hence, ablation width was related to the thermalization area corresponding to solid/liquid phase transition, where either the melting temperature T_m of Cu (1357.8 K, utilized in Fig. 6b) or the superheating temperature $T_{hm} = 1.37 \times T_m$ associated with ultrafast homogeneous melting within the time period of $\tau_{eq} \approx 4$ ps is considered in numerical simulation [55], to parallelly allow for comparison and evaluation of the applicability of the ultrafast homogeneous melting theory in this study. The course of ablation area expanse in Fig. 6b that is corresponding to substrate thermalization up to T_m without involvement of A_x does not exhibit a significant difference between s- and p-polarization for both 6 µm and 3 µm in case of 2.1 J/cm^2. At 750 nm periodicity, on the other hand, chemical incubation alone suffices to enhance p-pol over s-pol ablation at 1.4 J/cm^2. In contrast to topography insensitive simulation, experimental measurements exhibit characteristic kinks of dropping ablation area width with increasing pulse count, which cannot be mirrored without the involvement of topographical effects on localized absorptance. Consistently, the results achieved by numerical simulation applying A_x follow similar trends like the experimental values even achieving similar results at maximal N for 60% of the patterns, which emphasizes a mutual influence of topographic surface modification and laser/material interaction. The clear deviation between experimental and numerically calculated ablation width in Fig. 6b can be attributed to the pure consideration of the thermalization zone in FEM simulation without including melt-kinetics in the resulting ablation process additionally expanding the melt-affected area.

Pattern scales of 6 µm show a weaker effect of polarization specific absorptance amplification, which is visible in both experimental and calculated ablation width and can be directly linked to lower aspect ratios at similar pulse counts. This accounts to both ablation width enhancement and initial difference in ablation rate between s-pol and p-pol due to a comparably low partial beam incidence angle. Polarization specific ablation is well-expressed for 3 µm, in contrast, exhibiting characteristic kinks in ablation area expansion at $N = 2$ for s-pol and $N = 5$ for p-pol in both experimental and calculated values involving topographic alteration of localized absorptance. The deviation between both numerical calculations of substrate thermalization at $N = 10$ especially for s-pol is additionally highlighted in Fig. 6c, where the difference of thermalization width up to T_{hm} is marked for both s-pol and p-pol. The importance of involving the irradiation incidence angle to correctly model absorptance is especially apparent for 750 nm pattern periodicity, where calculated p-pol ablation width either match or underestimate experimental results depending on the involvement of A_x. Here, the effect of p-pol on ablation area expanse is already apparent after the first pulse, as visible in Fig. 6b with less significance for s-pol. Further processing finally induces melt-overlap for p-pol and shrinking ablation width for s-pol considering substrate thermalization alone. Comparing thermalization between T_m and T_{hm} for 750 nm patter periodicity, it has to be emphasized that only the latter correctly predicts a full overlap of the molten areas corresponding to pattern deterioration in the experimental results at $N = 3$ (compare Fig. 6b, d and e). This indicates a good correlation of T_{hm} with actual ablation related substrate thermalization when combined with incubation related laser/material

interaction in numerical calculation. The considerable deviation of both simulated s-pol values from experimental data highlight the additional effect of melt-agitation in ablation area expansion at this pattern scale, as visible in the topographic morphologies displayed in Fig. 2d. As soon as ablation area separation breaks down by melt-overlap, the DLIP induced pattern gets deteriorated, where surface morphology rather exhibits sub-pattern crater features also visible in the ablation area of µm-scaled USP-DLIP patterns. While topography/polarization dependent laser/material interaction has been shown to significantly affect primary topography, sub-pattern formation might similarly be impacted by DLIP alongside multi-pulse processing.

3.2.5. *Sub-pattern morphology*

The morphology of sub-pattern craters for varying processing parameters has been investigated by means of statistical segmentation based on watershed algorithm utilizing high-contrasted SEM images of 3 µm and 6 µm patterned single laser spots. The investigated morphologic features involving crater size and shape factors (displayed in Fig. 7e) have been chosen to determine multi-pulse response mechanisms in sub-pattern formation alongside primary USP-DLIP. The effect of low- and mid-fluence irradiation has been analyzed for 3 µm periodicity including 0.76 J/cm^2, 2.1 J/cm^2 and 3.37 J/cm^2, while a comparison of 3 µm and 6 µm at 2.1 J/cm^2 involves the influence of pattern scale on crater formation.

Comparing the lower graphs in Fig. 7a-c, initial crater size is showing minor fluence regime specific difference. According to thermal simulation from previous work, spallation ablation can be assumed as the predominant ablation mechanism in first pulse ablation leading to less crater-like ablation features as visible in Fig. 2b-d. In case of mid-fluence regime irradiation, the dominant ablation mechanism changes to phase explosion after the second pulse [16]. Likewise, crater size gets enhanced alongside ongoing pulse accumulation with a shallow slope

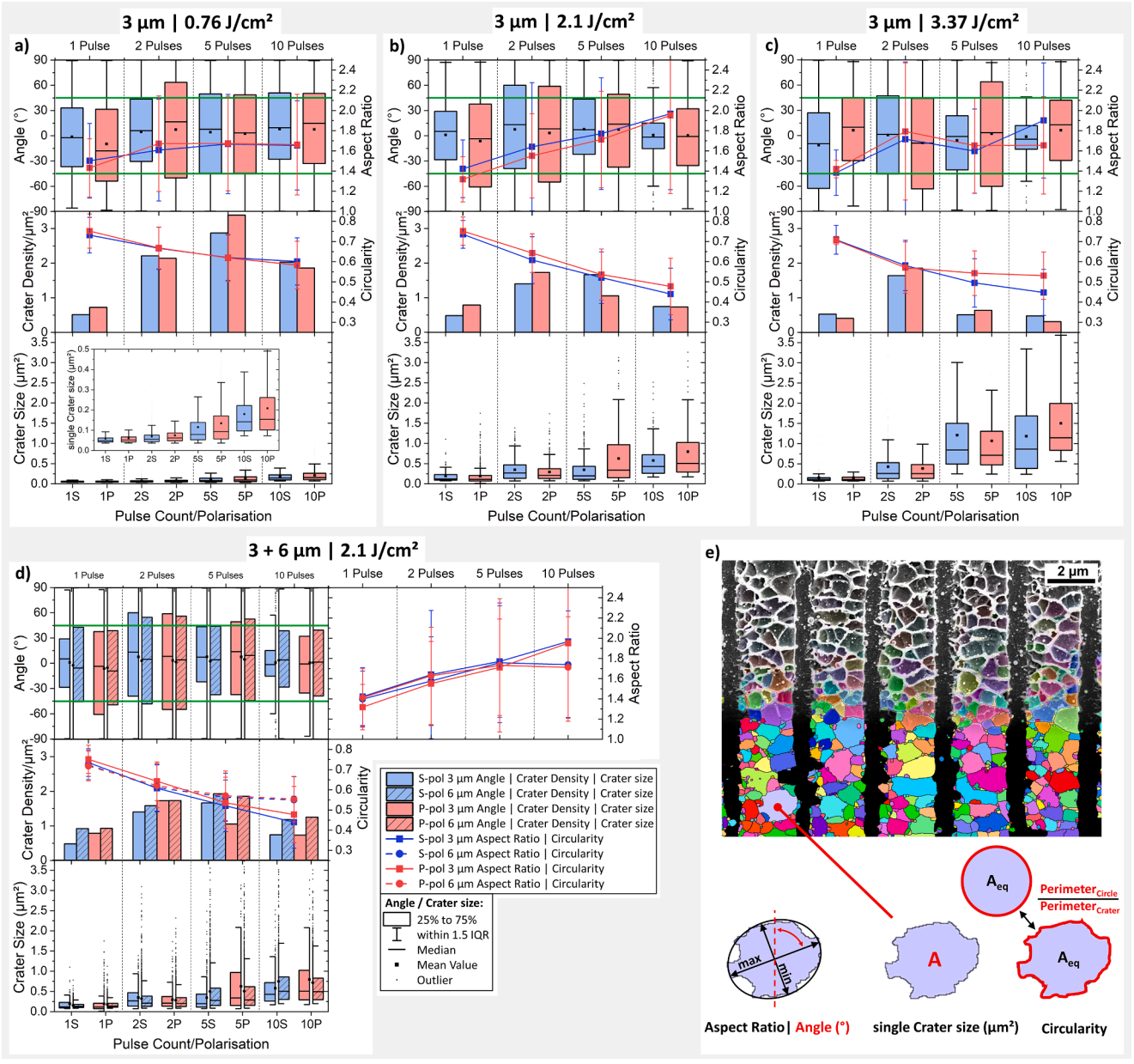

Fig. 7. Statistical segmentation of sub-pattern crater morphology utilizing high contrasted SEM images and watershed algorithm. Crater morphologies are plotted in combined graphs in case of correlated parameters comparing the effect of a) 0.76 J/cm^2, b) 2.1 J/cm^2 and c) 3.37 J/cm^2 fluence at 3 µm periodicity as well as pattern scale between d) 3 µm and 6 µm periodicity at 2.1 J/cm^2 on sub-pattern formation. e) Schematic illustration of the analytical procedure involving the investigated morphological parameters.

for 0.76 J/cm^2 while this behavior is well-pronounced for 2.1 J/cm^2 and especially 3.37 J/cm^2, also indicating a higher pulse-wise increase of absorptance of the modified surfaces. In the mid-fluence regime, the increase in crater size appear to saturate between $N = 5$ and 10 exhibiting higher values for p-pol, while s-pol dominates in crater size after the second pulse. The latter aspect builds an interesting parallel to the inverted absorptance relation between s-pol and p-pol for $N = 2$ in the UV–Vis results after deoxidation. In case of further ablation at 0.76 J/cm^2, crater size increases almost linearly with pulse count on a low scale with consistently higher crater sizes for p-pol, indicating a prevailing dominance of spallation. The falling slope of crater density for increasing pulse agglomeration after $N = 5$ for 0.76 J/cm^2 as well as $N = 2$ for 2.1 J/cm^2 and 3.37 J/cm^2 is directly linked to the continuously increasing crater size, due to the limited space available within the ablation area. Arising from the physical constriction by neighboring craters and the topographical pattern boundaries, radially expanding crater edges merge into a cellular network reducing the circularity of the individual crater shape (visible in Fig. 7e). Further pulsing decreases crater density independent of the utilized laser parameters as soon as circularity falls below 0.6 indicating a recombination of individual craters alongside crater size enhancement in the highly connected sub-pattern mesh. Based on this, the development of crater shape allows to detect preferred expansion/recombination angles depending on primary pattern topography and beam polarization.

Increasing crater aspect ratio is plotted in relation to the orientation angle of the major axis, where 0° is oriented parallel to the line-like pattern and exhibits the preferential orientation angle of crater elongation relative to both beam polarization and the pattern topography. The boxes of the statistical graph represent 50% of the measured values closest related to 0° orientation, by which an overlap with the thresholds of ±45° (highlighted by the green lines) mark preferential perpendicular (90°) overall crater orientation relative to the pattern topography, while no overlap indicates rather parallel (0°) elongation. Closely linked to falling circularity, the aspect ratio of the individual craters increases almost to the same extent for both s- and p-polarization, with higher aspect ratio/lower circularity for s-pol after $N = 10$ in the mid-fluence regime. Here, the elongated s-pol craters are aligned almost parallel to the line-like primary pattern geometry already after the 5th pulse indicating an increasing influence of the lowered ablation area width of the primary pattern at higher pulse counts. A similar effect is also apparent for $N = 10$ in case of p-pol, where the later inset of this behavior follows the same trend as primary pattern formation in relation to localized absorptance A_x. An influence of either the beam polarization or pattern topography on crater orientation is not visible at 0.76 J/cm^2, while slightly higher crater sizes might be linked to preferential p-pol absorption. This might be resulting from both the low pattern aspect ratio and crater expansion at this state of processing for the low fluence regime.

Directly comparing pulse-wise alteration of crater orientation to corresponding primary pattern geometries highlights a paralleled relation between high ablation width and majorly perpendicular crater orientation for p-pol as well as stabilizing lower ablation width and pronounced parallel orientation for s-pol. From this, an influence of polarization related absorptance on topography slopes appears to be effective on sub-pattern features similarly to the already shown impact on primary pattern formation.

To better illuminate this phenomenon, a comparison of crater morphology segmentation was performed on USP-DLIP patterns of 3 µm and 6 µm periodicity with increasing pulse count at a uniform fluence of 2.1 J/cm^2. Here, the slopes of crater density, circularity and aspect ratio alongside increasing pulse count on 6 µm patterns follow a similar trend like the low-fluence regime patterns at 3 µm periodicity, however with higher crater size linked to the fluence. For similar fluence applied, crater size is constantly higher on 3 µm and increases additionally in difference at $N = 5$ for p-pol, whereas the ratio between 3 µm and 6 µm crater size gets inverted at this pulse count for s-pol. In parallel, both crater density and circularity of the 3 µm patterns fall increasingly below the values of 6 µm at this state of pulse agglomeration alongside higher aspect ratio and a more pronounced crater orientation parallel to the pattern geometry. The combined alteration in crater morphology parameters between the two pattern scales after $N = 5$ highlights the significant effect of primary pattern topography on sub-pattern formation: Higher pattern scales exhibit a smaller increase in primary pattern aspect ratio within the ten first consecutive pulses, while at 3 µm periodicity the topography induced alteration in absorptance is already stronger expressed, which appears to also affect sub-pattern formation, as visible by comparison of the s- and p-pol crater size relation between 3 µm and 6 µm. In parallel, the increased topography slope on 3 µm patterns after $N = 5$ focusses surface excitation at the ablation area centers while the steepening topography limits perpendicular crater expanse. However, beam polarization appears to also affect crater morphology at lower pulse counts before it gets affected by the primary pattern topography as visible in the pronounced perpendicular p-pol crater orientation independent of pattern scale. The overall widening of crater diameter appears to be preferentially aligned in perpendicular orientation to the beam polarization, which fits to the polarization relation of localized absorptance A_x and correlates with common LSFL formation theory [19]. Preferential localized absorption within the crater-like network of the initial sub-pattern topography at 0.76 J/cm^2 thus appears to be involved in the transformation to LSFL sub-pattern morphology after higher pulse counts as observed in planar patterning at accumulated 21 J/cm^2 (see Fig. 3).

As an additional effect, 3 µm ablation area width is in lower size-relation to the pulse-wise increasing sub-pattern crater size in the mid-fluence regime, by which the bottom profile of the ablation area at $N = 10$ is majorly related to single craters, especially for s-pol at 2.1 J/cm^2 and 3.37 J/cm^2 (see Fig. 2c). The effect of low primary/sub-pattern feature size relation is further amplified in the case of 750 nm compared to 3 µm periodicity, whereas incubation induced increase in crater size might invert the dominance in topography formation between primary and sub-pattern. The Cu-specific incubation impact on ablation kinetics appears to cause the previously observed low fluence/pulse count threshold for qualitative processing at sub-µm pattern scale observed [16],[17]. This points out the need to consider sub-pattern formation alongside primary DLIP patterning in case of USP-DLIP on Cu for pattern scales <6 µm. Since crater size enhancement depends on laser energy absorption, threshold fluences to avoid negative interplay between primary and sub-pattern formation for USP-DLIP can be interpolated from the experimental results. Involving primary pattern size and the specific incubation behavior, the polarization dependent threshold fluences for high USP-DLIP pattern quality on Cu correspond to $F_s \approx P$ and $F_p \approx 2/3\ P$ (in J/cm^2 and µm). However, additional effects on laser/substrate interaction, like e.g. a reduced absorption of s-pol USP-DLIP irradiation at high single beam incidence angles for sub-µm pattern scales have to be considered in parallel, where higher fluences need to be applied to achieve ablation.

4. Conclusions

The geometry and morphology of USP-DLIP patterns on Cu have been shown to be dependent on different ablation mechanisms in the low- and mid-fluence regime as well as pattern scale in parallel interaction of primary and sub-pattern formation. Within the first 2 to 10 consecutive pulses, pattern geometry formation and chemical surface conditioning is initiated, which predominantly influences further USP-DLIP processing and the resulting pattern morphology. Here, the underlying mechanisms in pattern formation are related to beam polarization involving both interference pattern modulation, as well as altering absorptance by pulse wise substrate modification that play an interconnected role.

Incubation during USP-DLIP processing of Cu turns out to be too complex to allow the application of general methodology based on

Gaussian spot examination. This is mainly due to the combined impact of beam polarization and primary pattern topography on localized absorptance, but also relates to sub-pattern formation mechanisms in case of smaller pattern periodicities scaling close to the sub-pattern feature sizes. To better understand the contribution of incubation mechanisms on multi-pulse USP-DLIP pattern formation, the individual incubation mechanisms have been selectively investigated:

- Between the different individual influences on incubation, surface oxidation, both as passivation layer and process-induced, has the highest impact on initial absorptance and its pulse wise increase during USP-DLIP processing of Cu at a wavelength of 800 nm. The results highlight the impact of initial substrate condition on laser processing also including its deformation state, which must be considered in laser parametrization. Directly related to the extent of ablative interaction, incubation by oxidic agglomeration scales higher in the mid- compared to the low-fluence regime. Since oxide agglomeration also covers previously unprocessed surface compartments, the resulting enhancement of initial absorptance must be considered in pattern formation, as well. In low-fluence processing, oxidic pre-conditioning leads to higher initial aspect ratios, while at mid-fluence processing, pattern formation starts to get negatively affected with raising fluence in the case of 3 µm patterns. Here, melt-agitation during phase explosion is enhanced alongside the increasing surface absorptance, which causes the affection of pattern peaks in both s- and p-pol multi-pulse USP-DLIP processing.
- Incubation by crystallographic defect formation mainly plays a role on deformation free Cu surfaces exhibiting low initial absorptance of 0.036 at 800 nm. In contrast, mechanical polishing already induces a defect related increase of absorptance, which is barely surpassed during multi-pulse USP-DLIP processing. This might be linked to the upper limit of dislocation density in crystallographic deformation of Cu, which appears to be closely approximated in polishing already, whereby sufficient defect formation during laser processing to considerably contribute to incubation cannot be accumulated. Here, the impact of surface oxide on overall absorptance can again be observed, as immersion etched samples exhibit reduced ablative interaction compared to their as-polished counter parts. Low-fluence USP-DLIP was applied at increased pulse counts close to the corresponding multi-pulse ablation threshold to investigate the impact of crystallographic substrate condition on incubation. Here, preferentially enhanced incubation by defect implantation on annealed Cu surfaces could be linked to preferential crystallographic orientations, where ablative interaction scales with a relation of {111} > {110} > > {100}. The course of defect related incubation includes HSFL formation, followed by further enhancing spallative ablation, both expanding from the ablation area center outwards along the descending slope of the intensity pattern in case of low-fluence USP-DLIP irradiation. Here, a certain topographic effect on absorptance by HSFL formation might as well be involved alongside further pronouncing sub-pattern formation due to the nano-scaled feature size [54]. In the case of mechanically polished Cu exhibiting significantly increased initial absorptance, ablation induces considerable LSFL formation correlating to low-fluence regime pattern morphology after twice the pulse count. Here, LSFL formation appears to be the main mechanism involved in pattern formation for s-pol at sub-threshold fluence.
- Incubating effects of topography alteration unrelated to beam polarization have mainly been observed for nm-scaled sub-pattern morphologies after the first laser pulse, where the relation between feature size and laser wavelength induce enhanced absorptance [54]. This is visible in both the significant increase of ablation width as well as the drop of measured absorptance in UV–Vis spectroscopy on immersion etched samples after the second consecutive pulse. Increasing sub-pattern feature size, especially related to phase explosion ablation, appear to reduce topography induced overall absorptance, but rather follow polarization sensitive localized absorptance during pulse wise sub-pattern formation similarly to the primary pattern.
- The formation of the primary line-like pattern proves to be predominantly dependent on beam polarization in direct interaction with pulse-wise surface modification. Comparison to experimental data exhibits the applicability of the introduced numerical model to determine pulse wise substrate thermalization corresponding to locally increased absorptance A_x and pattern formation, which allows for a better interpretation of the impact of the different incubation mechanisms. Absorptance is increased alongside topography edges in perpendicular orientation to the beam polarization, which favors ablation area expanse for p-pol and ablation depth increase for s-pol in case of µm-scaled USP-DLIP patterns. Reaching aspect ratios above 0.4, absorptance at the edge of the ablation area also decreases for p-pol inducing a trend of inverted ablation area expanse similar to s-pol ablation. Pattern peaks appear to also suffer partial ablation at higher fluences in case of p-pol at 3 µm pattern periodicity due to the lesser modulated interference minima in combination with a pre-conditioning of the pattern peaks increasing the local absorptance. In contrast, higher pattern depths are achieved for p-pol at sub-µm pattern scales in inverse relation to intensity modulation, where melt pile-ups can contribute to pattern formation but become destabilized in case of further pulse agglomeration. Multi-pulse sub-µm pattern stability is improved in case of low-fluence regime USP-DLIP processing due to decreased melt-agitation and reduced oxidic agglomeration.
- Sub-pattern formation is predominantly determined by the specific ablation mechanisms induced by USP irradiation of Cu. The initial sub-pattern morphology is characterized by crater-like features, which align into a mesh-like network along consecutive pulsing. Depending on the ablation mechanism prevailing throughout incubation, crater-sizes significantly increase in case of phase explosion, by which they tend to merge with the primary pattern at low primary/sub-pattern feature size ratio especially in the mid-fluence regime. In the case of spallative ablation, the mesh-like sub-pattern may transform into LSFL at higher pulse counts in the low-fluence regime. Alteration of crater morphology is governed by polarization dependent reshaping similar to LSFL formation and alignment along primary pattern scales in case of sufficiently high aspect ratios.
- Alongside primary and sub-pattern formation, beam polarization has been shown to also impact initial absorption in relation to the partial beam incidence angle. This leads to polarization specific ablation efficiency in inverse relation to the actual difference in interference modulation between s-pol and p-pol. This effects scales higher with decreasing pattern scale due to enhanced single beam incidence angles [36], by which single and multi-pulse ablation thresholds effective in USP-DLIP patterning scale above in case of p-pol and below the corresponding values calculated using incubation models relating on Gaussian spot experiments, in case of s-pol. According to these findings, single beam interaction with the substrate surfaces also impacts DLIP processing alongside interference pattern formation, which has not been considered, so far.

In summary, pattern geometry and morphology formation on Cu in response to USP-DLIP underlies a complex interplay of mutually interacting multi-pulse agglomeration effects impacting the development of both primary and sub-pattern. Based on our findings, polarization dependent locally increased absorptance alongside topographic and chemical surface modification plays a similar critical role as intensity pattern modulation by interference. Hence, laser/material interaction in USP-DLIP is defined by the superposition of both intensity and absorptance modulation alongside multi-pulse processing, which as well affects initial surface and partial beam properties. By determining the impact of the individual agglomeration effects related to the specific optical and physical properties of Cu, these findings can be used as a foundation to

improve the understanding of multi-pulse USP-DLIP of other metallic materials, as well. Using this knowledge, increased precision in targeted micro- and nanometer scaled surface pattering via laser interference inducing higher impacts of surface functionalization in the manifold application areas previously mentioned can be realized.

Author contributions

D.W. Müller conceived the idea, designed the interference-based laser setup, developed the numerical model and conducted the numerical analyzation. Sample preparation, surface characterization via confocal laser scanning microscopy (LSM) and scanning electron microscopy (SEM) as well as morphologic segmentation were performed by D.W. Müller and S. Lößlein. D.W. Müller and M. Briesenick conducted UV–Vis Spectroscopy. C. Pauly executed electron back-scatter diffraction analysis. Data interpretation and preparation of the manuscript was done by D.W. Müller. S. Lößlein and C. Pauly contributed in editing the manuscript. F. Mücklich and G. Kickelbick supervised the work.

Declaration of Competing Interest

The authors declare that they have no known competing financial interests or personal relationships that could have appeared to influence the work reported in this paper.

Data availability

Data will be made available on request.

Acknowledgements

The authors acknowledge financial support in the project “ZuMat” (supported by the Saarland State Chancellery with resources from the European Fund for Regional Development (EFRE)) and for the project “Pulsatec”(supported as part of the EFRE program Interreg Greater Region). Parts of this work were financially supported by the German Research Foundation (DFG) within the projects “Controlled bacterial interaction to increase the antimicrobial efficiency of copper surfaces” (project number 415956642) and “Influence of surface topography and chemistry on the wetting behavior of laser-structured metallic surfaces” (project number 435334669). The authors acknowledge funding for the PFIB/SEM instrument used for the EBSD measurements by Deutsche Forschungsgemeinschaft (DFG, INST 256/510-1 FUGG).

References

[1] A.F. Lasagni, C. Gachot, K.E. Trinh, M. Hans, A. Rosenkranz, T. Roch, S. Eckhardt, T. Kunze, M. Bieda, D. Günther, V. Lang, F. Mücklich, Direct laser interference patterning, 20 years of development: From the basics to industrial applications, in: Proc. SPIE 10092, Laser-Based Micro- Nanoprocessing XI, 2017, p. 1009211, https://doi.org/10.1117/12.2252595.

[2] H. Heffner, M. Soldera, A.F. Lasagni, Optical enhancement of fluorine-doped tin oxide thin films using infrared picosecond direct laser interference patterning, Adv. Eng. Mater. (2022) 2200266, https://doi.org/10.1002/adem.202200266.

[3] B. Voisiat, W. Wang, M. Holzhey, A.F. Lasagni, Improving the homogeneity of diffraction based colours by fabricating periodic patterns with gradient spatial period using direct laser interference patterning, Sci. Rep. 9 (2019) 7801, https://doi.org/10.1038/s41598-019-44212-4.

[4] A.M. Kietzig, M.N. Mirvakili, S. Kamal, P. Englezos, S.G. Hatzikiriakos, Laser-patterned super-hydrophobic pure metallic substrates: Cassie to Wenzel wetting transitions, J. Adhes. Sci. Technol. 25 (2011) 2789–2809, https://doi.org/10.1163/016942410X549988.

[5] P.G. Grützmacher, A. Rosenkranz, C. Gachot, How to guide lubricants – tailored laser surface patterns on stainless steel, Appl. Surf. Sci. 370 (2016) 59–66, https://doi.org/10.1016/j.apsusc.2016.02.115.

[6] A. Rosenkranz, L. Reinert, C. Gachot, F. Mücklich, Alignment and wear debris effects between laser-patterned steel surfaces under dry sliding conditions, Wear. 318 (2014) 49–61, https://doi.org/10.1016/j.wear.2014.06.016.

[7] R. Schieber, C. Mas-Moruno, F. Lasserre, J.J. Roa, M.P. Ginebra, F. Mücklich, M. Pegueroles, Effectiveness of direct laser interference patterning and peptide immobilization on endothelial cell migration for cardio-vascular applications: an in vitro study, Nanomaterials. 12 (2022) 1217, https://doi.org/10.3390/nano12071217.

[8] J. Minguela, D.W. Müller, F. Mücklich, L. Llanes, M.P. Ginebra, J.J. Roa, C. Mas-Moruno, Peptidic biofunctionalization of laser patterned dental zirconia: a biochemical-topographical approach, Mater. Sci. Eng. C 125 (2021), 112096, https://doi.org/10.1016/j.msec.2021.112096.

[9] D.W. Müller, S. Lößlein, E. Terriac, K. Brix, R. Kautenburger, K. Siems, R. Möller, F. Mücklich, Increasing antibacterial efficiency of Cu surfaces by targeted surface functionalization via ultrashort pulsed direct laser interference patterning (USP-DLIP), Adv. Mater. Interfaces 8 (2021) 2001656, https://doi.org/10.1002/admi.202001656.

[10] K. Siems, D.W. Müller, L. Maertens, A. Ahmed, R. Van Houdt, R.L. Mancinelli, S. Baur, K. Brix, R. Kautenburger, N. Caplin, J. Krause, R. Demets, M. Vukich, A. Tortora, C. Roesch, G. Holland, M. Laue, F. Mücklich, R. Moeller, Testing laser-structured antimicrobial surfaces under space conditions: the design of the ISS experiment BIOFILMS, Front. Sp. Technol. 2 (2022) 1–18, https://doi.org/10.3389/frspt.2021.773244.

[11] S. Indrišiūnas, B. Voisiat, M. Gedvilas, G. Račiukaitis, New opportunities for custom-shape patterning using polarization control in confocal laser beam interference setup, J. Laser Appl. 29 (2017), 011501, https://doi.org/10.2351/1.4976679.

[12] F. Fraggelakis, G.D. Tsibidis, E. Stratakis, Tailored sub-micrometer periodic surface structures via ultrashort pulsed direct laser interference patterning, Phys. Rev. B 103 (2021), 054105, https://doi.org/10.1103/physrevb.103.054105.

[13] F. Mücklich, A. Lasagni, D. Claus, Laser interference metallurgy – using interference as a tool for micro / nano structuring, Int. J. Mater. Res. 97 (2006) 1337–1344.

[14] B. Voisiat, C. Zwahr, A.F. Lasagni, Growth of regular micro-pillar arrays on steel by polarization-controlled laser interference patterning, Appl. Surf. Sci. 471 (2019) 1065–1071, https://doi.org/10.1016/j.apsusc.2018.12.083.

[15] B. Voisiat, S. Milles, A.F. Lasagni, Impact of molten pool dynamics on resultant surface structures during direct laser interference patterning, J. Laser Micro Nanoeng. 16 (2021) 1–6, https://doi.org/10.2961/jlmn.2021.01.2006.

[16] D.W. Müller, T. Fox, P.G. Grützmacher, S. Suarez, F. Mücklich, Applying ultrashort pulsed direct laser interference patterning for functional surfaces, Sci. Rep. 10 (2020) 3647, https://doi.org/10.1038/s41598-020-60592-4.

[17] M. Bieda, M. Siebold, A. Fabián, Applied Surface Science Fabrication of sub-micron surface structures on copper, stainless steel and titanium using picosecond laser interference patterning, Appl. Surf. Sci. 387 (2016) 175–182, https://doi.org/10.1016/j.apsusc.2016.06.100.

[18] Y. Fuentes-Edfuf, J.A. Sánchez-Gil, C. Florian, V. Giannini, J. Solis, J. Siegel, Surface plasmon polaritons on rough metal surfaces: role in the formation of laser-induced periodic surface structures, ACS Omega. 4 (2019) 6939–6946, https://doi.org/10.1021/acsomega.9b00546.

[19] J. Bonse, S. Gräf, Maxwell meets marangoni—a review of theories on laser-induced periodic surface structures, Laser Photonics Rev. 14 (2020) 1–25, https://doi.org/10.1002/lpor.202000215.

[20] A. Rudenko, A. Abou-Saleh, F. Pigeon, C. Mauclair, F. Garrelie, R. Stoian, J. P. Colombier, High-frequency periodic patterns driven by non-radiative fields coupled with Marangoni convection instabilities on laser-excited metal surfaces, Acta Mater. 194 (2020) 93–105, https://doi.org/10.1016/j.actamat.2020.04.058.

[21] A. Sikora, M. Faucon, L. Gemini, R. Kling, G. Mincuzzi, LIPSS and DLIP: from hierarchical to mutually interacting, homogeneous, structuring, Appl. Surf. Sci. 591 (2022), 153230, https://doi.org/10.1016/j.apsusc.2022.153230.

[22] F. Fraggelakis, G.D. Tsibidis, E. Stratakis, Ultrashort pulsed laser induced complex surface structures generated by tailoring the melt hydrodynamics, Opto-Electron. Adv. 5 (2022), 210052, https://doi.org/10.29026/oea.2022.210052.

[23] K.K. Anoop, R. Fittipaldi, A. Rubano, X. Wang, D. Paparo, A. Vecchione, L. Marrucci, R. Bruzzese, S. Amoruso, Direct femtosecond laser ablation of copper with an optical vortex beam, J. Appl. Phys. 116 (2014), 113102, https://doi.org/10.1063/1.4896068.

[24] Y. Jee, M.F. Becker, R.M. Walser, Laser-induced damage on single-crystal metal surfaces, J. Opt. Soc. Am. B. 5 (1988) 648–659, https://doi.org/10.1364/josab.5.000648.

[25] G. Raciukaitis, Ultra-short pulse lasers for microfabrication: a review, IEEE J. Sel. Top. Quantum Electron. 27 (2021) 1100112, https://doi.org/10.1109/JSTQE.2021.3097009.

[26] S.E. Kirkwood, A.C. Van Popta, Y.Y. Tsui, R. Fedosejevs, Single and multiple shot near-infrared femtosecond laser pulse ablation thresholds of copper, Appl. Phys. A Mater. Sci. Process. 81 (2005) 729–735, https://doi.org/10.1007/s00339-004-3135-7.

[27] A.Y. Vorobyev, C. Guo, Reflection of femtosecond laser light in multipulse ablation of metals, J. Appl. Phys. 110 (2011), 043102, https://doi.org/10.1063/1.3620898.

[28] S.M. Lößlein, M. Kasper, R. Merz, C. Pauly, D.W. Müller, M. Kopnarski, F. Mücklich, Patience alone is not enough - a guide for the preparation of low-defect sections from pure copper Geduld allein reicht nicht! - Ein Leitfaden zur Herstellung defektarmer Schliffe von Reinkupfer, Prakt. Metallogr. Metallogr. 58 (2021) 388–407, https://doi.org/10.1515/pm-2021-0031.

[29] D.W. Müller, A. Holtsch, S. Lößlein, C. Pauly, C. Spengler, S. Grandthyll, K. Jacobs, F. Mücklich, F. Müller, In-depth investigation of copper surface chemistry modification by ultrashort pulsed direct laser interference patterning, Langmuir. 36 (2020) 13415–13425, https://doi.org/10.1021/acs.langmuir.0c01625.

[30] N. Habbache, N. Alane, S. Djerad, L. Tifouti, Leaching of copper oxide with different acid solutions, Chem. Eng. J. 152 (2009) 503–508, https://doi.org/10.1016/j.cej.2009.05.020.

[31] J. Schille, L. Schneider, U. Loeschner, Process optimization in high-average-power ultrashort pulse laser microfabrication: how laser process parameters influence efficiency, throughput and quality, Appl. Phys. A Mater. Sci. Process. 120 (2015) 847–855, https://doi.org/10.1007/s00339-015-9352-4.
[32] P.T. Mannion, J. Magee, E. Coyne, G.M. O'Connor, T.J. Glynn, The effect of damage accumulation behaviour on ablation thresholds and damage morphology in ultrafast laser micro-machining of common metals in air, Appl. Surf. Sci. 233 (2004) 275–287, https://doi.org/10.1016/j.apsusc.2004.03.229.
[33] C.W. Cheng, S.Y. Wang, K.P. Chang, J.K. Chen, Femtosecond laser ablation of copper at high laser fluence: modeling and experimental comparison, Appl. Surf. Sci. 361 (2016) 41–48, https://doi.org/10.1016/j.apsusc.2015.11.055.
[34] Y. Ren, J.K. Chen, Y. Zhang, Optical properties and thermal response of copper films induced by ultrashort-pulsed lasers, J. Appl. Phys. 110 (2011) 1–7, https://doi.org/10.1063/1.3662897.
[35] A.D. Rakic, A.B. Djuris, J.M. Elazar, M.L. Majewski, Optical properties of metallic films for vertical-cavity optoelectronic devices, Appl. Opt. 37 (1998) 5271–5283.
[36] S. Amoruso, X. Wang, C. Altucci, C. De Lisio, M. Armenante, R. Bruzzese, R. Velotta, Thermal and nonthermal ion emission during high-fluence femtosecond laser ablation of metallic targets, Appl. Phys. Lett. 77 (2000) 3728–3730, https://doi.org/10.1063/1.1329869.
[37] S. Indrišiūnas, B. Voisiat, M. Gedvilas, G. Račiukaitis, Polarisation control in direct laser interference ablation setup for flexible generation of periodic patterns, Proc. LPM2017 (2017) 1–5. http://www.jlps.gr.jp/lpm/lpm2017/.
[38] D. Legland, I. Arganda-Carreras, P. Andrey, MorphoLibJ: integrated library and plugins for mathematical morphology with ImageJ, Bioinformatics. 32 (2016) 3532–3534, https://doi.org/10.1093/bioinformatics/btw413.
[39] C.A. Schneider, W.S. Rasband, K.W. Eliceiri, NIH image to ImageJ: 25 years of image analysis, Nat. Methods 9 (2012) 671–675, https://doi.org/10.1038/nmeth.2089.
[40] J. Winter, M. Spellauge, J. Hermann, C. Eulenkamp, H.P. Huber, M. Schmidt, Ultrashort single-pulse laser ablation of stainless steel, aluminium, copper and its dependence on the pulse duration, Opt. Express 29 (2021) 14561, https://doi.org/10.1364/oe.421097.
[41] P. Simon, J. Ihlemann, Ablation of submicron structures on metals and semiconductors by femtosecond UV-laser pulses, Appl. Surf. Sci. 109–110 (1997) 25–29, https://doi.org/10.1016/S0169-4332(96)00615-0.
[42] A. Blumenstein, M.E. Garcia, B. Rethfeld, P. Simon, J. Ihlemann, D.S. Ivanov, Formation of periodic nanoridge patterns by ultrashort single pulse UV laser irradiation of gold, Nanomaterials. 10 (2020) 1998, https://doi.org/10.3390/nano10101998.
[43] C. Gattinoni, A. Michaelides, Atomistic details of oxide surfaces and surface oxidation: the example of copper and its oxides, Surf. Sci. Rep. 70 (2015) 424–447, https://doi.org/10.1016/j.surfrep.2015.07.001.
[44] P.P. Rajeev, S. Sengupta, A. Das, P. Taneja, P. Ayyub, P.K. Kaw, G.R. Kumar, Laser absorption in short-lived metal and nanoplasmas, Appl. Phys. B Lasers Opt. 80 (2005) 1015–1019, https://doi.org/10.1007/s00340-005-1827-0.
[45] P. Buffat, J.P. Borel, Size effect on the melting temperature of gold particles, Phys. Rev. A 13 (1976) 2287–2298, https://doi.org/10.1103/PhysRevA.13.2287.
[46] N. Tsakiris, K.K. Anoop, G. Ausanio, M. Gill-Comeau, R. Bruzzese, S. Amoruso, L. J. Lewis, Ultrashort laser ablation of bulk copper targets: dynamics and size distribution of the generated nanoparticles, J. Appl. Phys. 115 (2014), 243301, https://doi.org/10.1063/1.4885196.
[47] M. Hans, A. Erbe, S. Mathews, Y. Chen, M. Solioz, F. Mücklich, Role of copper oxides in contact killing of bacteria, Langmuir. 29 (2013) 16160–16166, https://doi.org/10.1021/la404091z.
[48] I. Platzman, R. Brener, H. Haick, R. Tannenbaum, Oxidation of polycrystalline copper thin films at ambient conditions, J. Phys. Chem. C 1101–1108 (2008).
[49] A.A. Ionin, S.I. Kudryashov, S.V. Makarov, P.N. Saltuganov, L.V. Seleznev, D. V. Sinitsyn, V.A. Lednev, S.M. Pershin, Electron emission and ultrafast low-fluence plasma formation during single-shot femtosecond laser surface ablation of various materials, JETP Lett. 101 (2015) 308–312, https://doi.org/10.1134/S0021364015050112.
[50] J. Vincenc Oboňa, V. Ocelík, J.C. Rao, J.Z.P. Skolski, G.R.B.E. Römer, A.J. Huis In 't Veld, J.T.M.D. Hosson, Modification of Cu surface with picosecond laser pulses, Appl. Surf. Sci. 303 (2014) 118–124, https://doi.org/10.1016/j.apsusc.2014.02.104.
[51] X. Sedao, M.V. Shugaev, C. Wu, T. Douillard, C. Esnouf, C. Maurice, S. Reynaud, F. Pigeon, F. Garrelie, L.V. Zhigilei, J.P. Colombier, Growth twinning and generation of high-frequency surface nanostructures in ultrafast laser-induced transient melting and resolidification, ACS Nano 10 (2016) 6995–7007, https://doi.org/10.1021/acsnano.6b02970.
[52] J.O. Porteus, D.L. Decker, J.L. Jernigan, W.N. Faith, M. Bass, 17.7 evaluation of metal mirrors for high-power applications by multi-threshold damage analysis, IEEE J. Quantum Electron. 14 (1977) 896–897, https://doi.org/10.1109/JQE.1977.1069587.
[53] Q. Xiong, Z. Li, T. Kitamura, Effect of crystal orientation on femtosecond laser-induced thermomechanical responses and spallation behaviors of copper films, Sci. Rep. (2017) 1–14, https://doi.org/10.1038/s41598-017-09559-6.
[54] A.Y. Vorobyev, C. Guo, Enhanced absorptance of gold following multipulse femtosecond laser ablation, Phys. Rev. B 72 (2005) 1–5, https://doi.org/10.1103/PhysRevB.72.195422.
[55] B. Rethfeld, K. Sokolowski-Tinten, D. von der Linde, S.I. Anisimov, Ultrafast thermal melting of laser-excited solids by homogeneous nucleation, Phys. Rev. B 65 (2002) 1–4, https://doi.org/10.1103/PhysRevB.65.092103.
[56] S.Y. Wang, Y. Ren, C.W. Cheng, J.K. Chen, D.Y. Tzou, Micromachining of copper by femtosecond laser pulses, Appl. Surf. Sci. 265 (2013) 302–308, https://doi.org/10.1016/j.apsusc.2012.10.200.